3. Results

3.1 Introductory Comments

Three different project stages were involved in the experimental work. These included (i) the successful preparation of thin alumina films, (ii) the synthesis and characterisation of the organometallic complex $Mo(C_3H_5)_4$ catalyst and (iii) the wet chemical combination of support and catalyst in UHV. In this chapter, therefore, I shall endeavour to present my results under the three main topics.

Sample preparation involved lengthy hot sputter cycles with Ar^+. Because of its affinity for surface contaminants such as C, S, and O and because of the significantly large concentrations of these contaminants in the bulk, Cr single crystals are notoriously difficult to clean in UHV. However, after several weeks of Ar^+ sputtering at elevated sample temperatures, a clean sample was obtained, as revealed by Auger and LEED measurements. Typical cleaning conditions included kinetic energies of 2.5 keV, Ar^+ partial pressure of $5 \cdot 10^{-4}$ mbar, sample temperatures between 800 and 1000 K, and sputtering episodes of approximately 1 hour between annealing and backfilling the chamber with more Ar. After about 100 hours of sputtering under the conditions listed above, a clean Cr(110) surface was obtained.

Three basic techniques exist for the preparation of thin oxide films in UHV[64,65]:

- oxidation of a metal single crystal
- evaporation of a foreign metal onto another metal or metal oxide substrate possibly within an oxygen atmosphere and
- the selective oxidation of single crystal alloys.

For the preparation of ordered thin alumina films, the third method has been successfully exploited by a number of groups[9,66,67]. For example, it has been known for some time that careful surface oxidation of (110)-oriented NiAl crystals yields ultrathin and ordered alumina films, but the presence of nickel complicates the structural elucidation of the thin

alumina films. The resulting complex structure of these films has been recently investigated in more detail and structural models have been proposed[68,69]. In the present work, a different approach was chosen, with the aim of generating ordered alumina films with a simple surface unit cell. To this end, a Cr(110) single crystal was carefully oxidised by using a procedure that is known to produce ordered films of $Cr_2O_3(0001)$[70,71]. Subsequently, $Al_2O_3(0001)$ was grown by the procedure described in the following sections.

3.2 Preparation of the $Al_2O_3(0001)$ support

In this section, I shall present AES, LEED, XPS and LEIS results on the preparation, structure and growth of the thin aluminium oxide films.

3.2.1 Cr(110) and $Cr_2O_3(0001)$ substrate

The procedure for generating a clean Cr(110) surface was already described in section 3.1 and will not be repeated here. AES and LEED did not indicate the presence of any contaminants (see fig. 3.1 and 3.2), and the LEED pattern of the clean surface was sharp (see below) and in line with previously published patterns of this surface. The oxidation of Cr was carried out according to standard procedures[7,71]. The clean Cr(110) surface was first annealed to 500 K and then exposed to $5 \cdot 10^{-6}$ mbar O_2 for 3 minutes. The sample temperature was increased to 598 K and oxygen dosed for 4 minutes at a partial pressure of $5 \cdot 10^{-7}$ mbar. The sample was annealed further to 773 K for 1 minute while keeping the oxygen partial pressure constant. Finally, the crystal was annealed to 1023 K for 2 minutes in $5 \cdot 10^{-7}$ mbar oxygen and then cooled down to 500 K whereby the oxygen supply was switched off. The crystal was allowed to cool down while the residual gases were pumped off. AE spectra and LEED pictures of the surface were taken immediately to avoid significant residual gas adsorption. The mean thickness of the oxide film, d, was deduced from the AES intensity ratio I_{Cr}^{3+}/I_{Cr}^{0} assuming the surface is completely covered by a film of uniform thickness[77,78,79]. The thickness of the oxide was estimated to be about 1.5 nm.

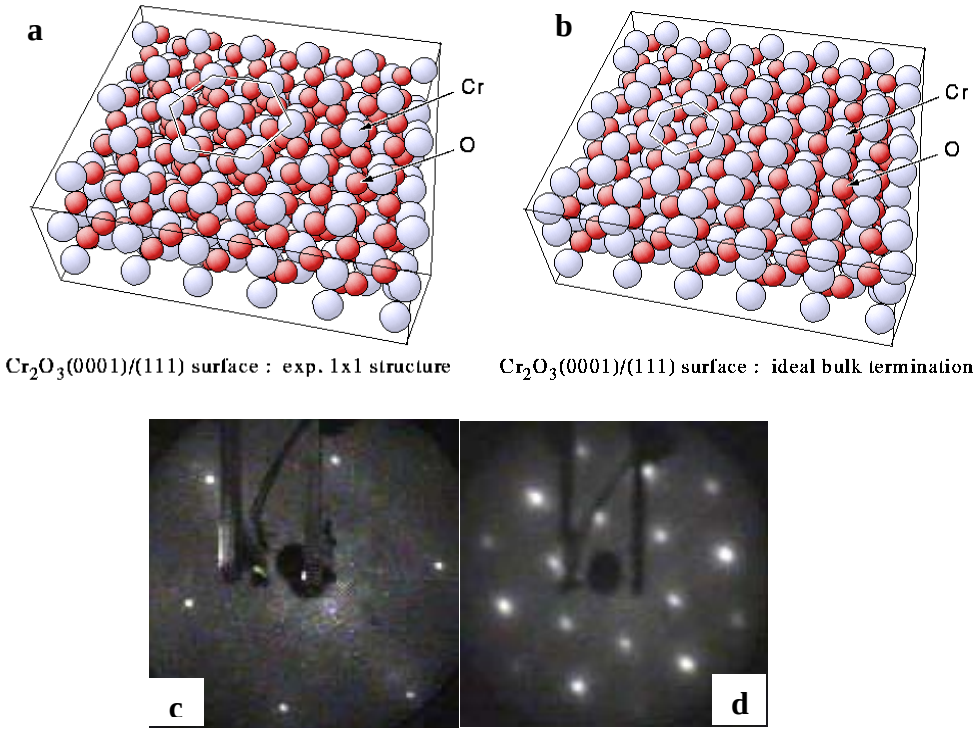

Figure 3.1: Experimentally determined and calculated Cr_2O_3 structures[76]; (c) and (d) are Cr(110) and Cr_2O_3(0001) measured at 69 eV beam energy respectively.

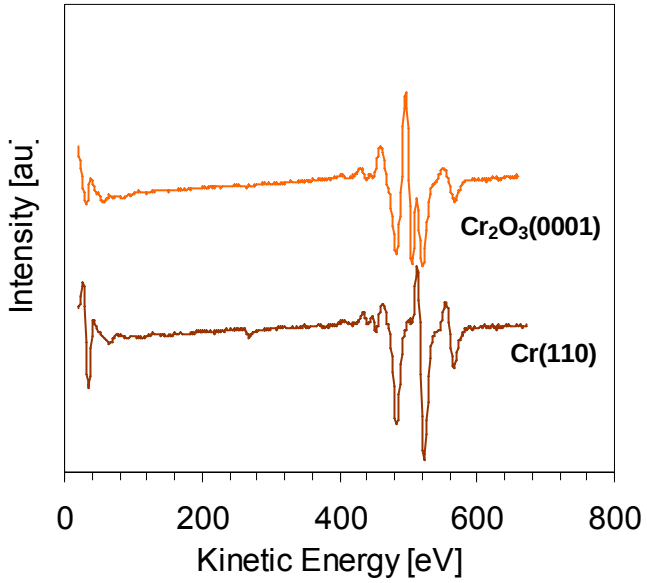

Figure 3.2: Survey AE spectra of (a) clean Cr and (b) Cr_2O_3 after exposing the former to O_2 and annealing to 1023 K.

The intensity ratio I_{Cr}^{3+}/I_{Cr}^{0} was estimated from figure 3.2 to be 0.33 using the peak-to-peak height of the 571 eV peak. Taking the IMFP for this electron in Cr to be 14.7 eV[79] and the CMA exit angle (available in the users' manual) to be 27°, the film thickness stated above was calculated using the equation:

$$\frac{I_{Cr^{3+}}}{I_{Cr^{0}}} = \frac{-d}{\lambda(E_k)\cos\vartheta} \tag{3.1}$$

where I_{Cr}^{3+} and I_{Cr}^{0} are the intensities of the Auger signals due to electrons with kinetic energy E_k after and before exposure of the clean surface to oxygen, respectively. λ is the IMFP of the 571 eV Auger electron and d is the thickness of the film.

The Cr(110) plane is the most densely packed bcc structure and seems to be the most reactive surface. This is manifested in the long Ar^+ sputtering at elevated temperatures (800-1000 K). The mechanism of the oxidation process has been well elucidated by previous studies[71,75]. The initial stages of Cr oxidation at lower temperatures (300-400 K) and O_2 partial pressures (around 10^{-7} Torr) give rise to streaking parallel to the 01 plane. Further oxygen exposure at 773 K and 10^{-6} Torr O_2 shows both streaks and diffraction spots. This has been explained as having to do with electron diffraction from both faceted domains and Cr(3×1)O structure domains[75]. The facets become less stable with increasing oxygen atmosphere. At 873 K and 10^{-6} Torr, the faceting is lost in favour of a new Cr(3×1) structure[75]. At this stage, the Cr surface exhibits the tendency to extend its rectangular symmetry while the oxygen layer tends to realise a hexagonal arrangement. This competition occurs in the 01 direction giving rise to elongated spots in this direction. Subsequent oxidation in 10^{-6} Torr O_2 at 1000 K gives rise to sharper spots and a six-fold symmetrical LEED pattern. The pattern does not change with additional heating or oxygen exposure, rather, the background intensity falls sharply[75]. The series of stages described above were not investigated in this work since we were only interested in the end product i.e., well ordered, epitactic Cr_2O_3 films. The oxygen exposed Cr(110) surface exhibited a characteristic (1×1) LEED pattern[76,77] of the Cr_2O_3(0001) surface.

Al evaporation experiments are described in the next section. More importantly, the resulting Cr_2O_3(0001) structure served as a template for the epitaxial growth of Al_2O_3(0001).

3.3 The Deposition of Aluminium at 300 K Followed by O_2 Exposure and Annealing to Higher Temperatures (AES)

3.3.1 Overview

The clean Cr_2O_3(0001) surface was exposed to Al vapour in ten minutes succession at 300 K, with the pressure in the chamber not exceeding $8 \cdot 10^{-10}$ mbar during the whole deposition period. Al deposition was followed by annealing and/or oxygen exposure at some stages. We shall call this the step-wise deposition method. Low energy (< 100 eV) AES and LEED were used to monitor the evolution of the resulting AlO_x films. The low energy Auger region was chosen because of the extreme surface sensitivity of these electrons. The results that will follow in the next section contain AES measurements of the step-wise deposition and oxidation series.

Figure 3.3 summarises a sequence of Al depositions and oxidations through a series of Auger electron spectra taken in the energy range between 20 and 70 eV (the most intense Al AE signals were observed in this range). It can be seen that the Cr MVV transitions gradually disappear and make room for the Al LVV transitions, which finally dominate the spectra. The complete absence of Cr signals in the final the spectra indicates the fact that segregation of Cr or intermixing of Cr and Al atoms in the alumina overlayer is negligible. The Cr-MVV signal at 37 eV is downshifted by 3 eV to 34 eV upon oxidation and at the same time strongly attenuated. Upon exposure to Al vapour at 300 K, the Al AE signal at 56 eV appears immediately. The energy position (56 eV) is indicative of the Al^{3+} valence state[7,78].

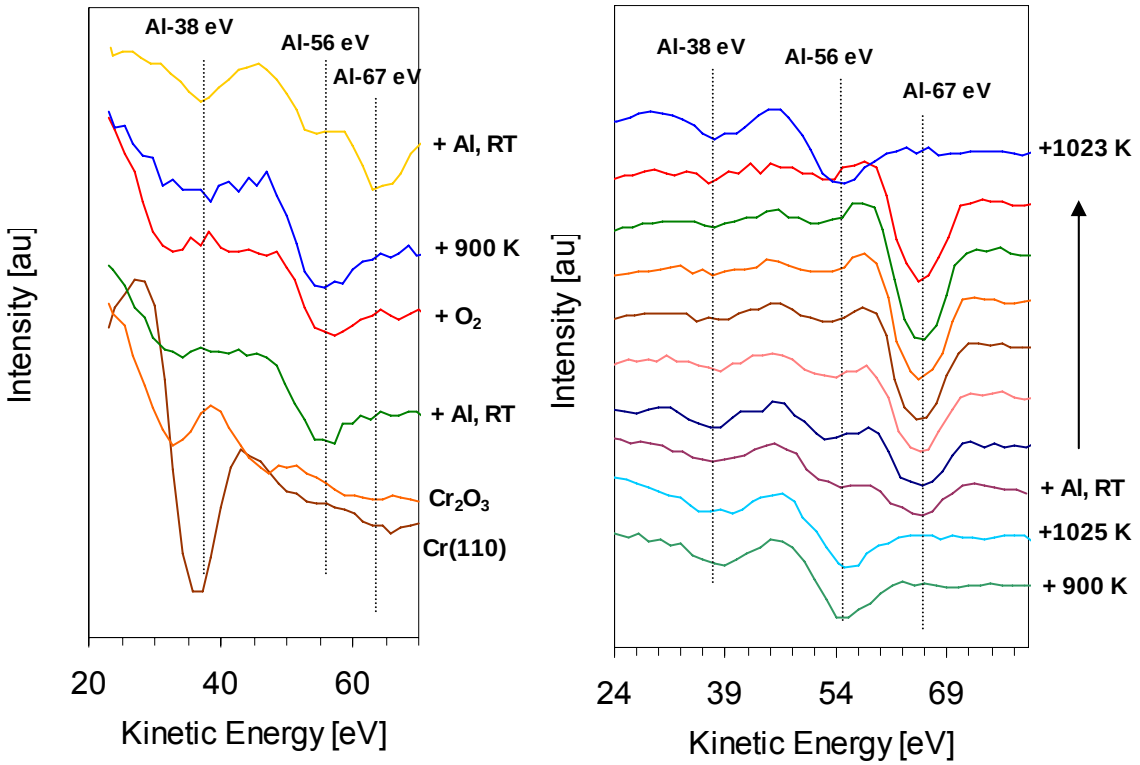

Figure 3.3: AE spectra of Al deposition followed by O_2 exposure and annealing. Each spectrum was recorded after a deposition time of 10 minutes using a cylindrical mirror analyser with an exit angle of 27°. The primary electron voltage was 2.5 keV with a filament current of 1 mA. The distance between electron source and sample was 8 mm.

Parallel LEED investigations reveal that the long range order of the substrate is no longer maintained at this stage. Exposing the sample to 5×10^{-7} mbar O_2 for 10 minutes did not lead to any visible change in the Al peak position. After annealing the sample to 900 K, the substrate structure was restored. Further evaporation of Al (topmost spectrum on the left) made, for the first time, a metallic Al AE signal at 67 eV appear. The long range order of the system was lost again and could not be restored even not after subsequent oxidation and annealing to 900 K and 1025 K, respectively (first and second bottom spectra on the right). Further Al depositions (third through penultimate spectrum) followed by O_2 exposure and annealing to 1023 K (topmost spectrum on the right) did not improve the situation. Oxidation and annealing led indeed to the disappearance of the huge Al signal at 67 eV, whilst the 38 and 56 eV signals (Al^{3+}) grew in intensity. This would imply that metallic Al has been fully converted to the (+III) valence state. The topmost Auger spectrum would

suggest the existence of pure epitaxially grown Al_2O_3, but LEED studies revealed that it was polycrystalline. This behavior demonstrates a severe disadvantage of the stepwise deposition/oxidation method, because it seems to be increasingly difficult to fully oxidise the deposited Al layers beyond a certain thickness, at least at the moderate oxygen partial pressures chosen in our experiments[74,80]. Under such conditions, it became difficult, if not impossible to obtain sufficiently well-ordered Al_2O_3 layers.

3.3.2 Co-deposition of aluminium and oxygen

We performed extensive experiments in which Al was evaporated in an ambient oxygen atmosphere onto the substrate while the latter was held at elevated temperatures. To be more specific, we evaporated Al metal onto the Cr_2O_3 (0001) substrate at 825 K at an oxygen partial pressure of 5×10^{-7} mbar. This temperature is quite critical, and we call it "epitactic", because epitactic growth between substrate and adsorbate only occurred in a narrow temperature window around 825 K, as revealed by parallel LEED experiments. Lower or higher substrate temperatures during deposition provided less ordered or even disordered alumina films.

3.3.2.1 Structure of the co-deposited films (LEED)

After every single Al deposition run the LEED patterns of the sample (substrate plus deposited alumina films) were monitored, while in parallel experiments, the chemical composition was also followed by Auger electron spectroscopy AES (see sect. 3.3.2.2). We did not observe any noticeable degradation of the film structure by electron bombardment, suggesting that the thin films were stable under the data acquisition conditions. This holds true for low-energy (LEED) as well as high-energy (AES) electron radiation. In figure 3.4, the LEED patterns observed during a typical deposition series are assembled, beginning with a clean Cr_2O_3(0001) substrate (fig. 3.4a) and ending with patterns of Al_2O_3 films of selected coverages (fig. 3.4b and 3.4c), taken at similar electron wavelengths to allow better comparison.

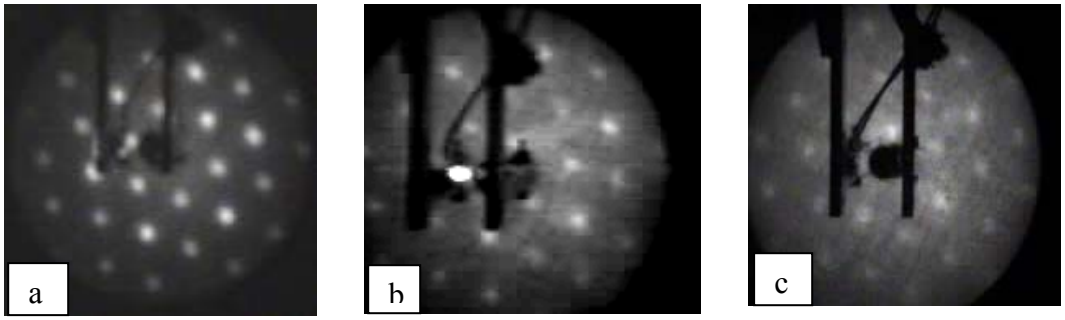

Figure 3.4: LEED pictures of the substrate and two Al_2O_3 covered samples measured at beam energy of 110 eV. b and c were obtained after the deposition of ca. 16 and 30 Å thick Al_2O_3 films respectively.

In detail, the LEED patterns shown refer to the clean Cr_2O_3(0001) substrate (a) and the 16 and 30 Å thick Al_2O_3 films (b) and (c), respectively. The excellent crystallographic quality of the chromia surface sample is evident from its LEED pattern and demonstrates that careful oxidation of the chromium single crystal surface leads to a well ordered epitactic oxide film. Directly after Al deposition, there was no evidence of a metallic aluminium superstructure. Instead, the hexagonal symmetry of the substrate was maintained as observed from LEED. Visible is the change in the quality of the patterns with increasing Al_2O_3 thickness. It is our assumption that the single-crystal character of the growing films decreases with increasing thickness; while the 16 Å thick film produces a very sharp LEED pattern with bright spots and weak background, the 30 Å film (although still very satisfactorily oriented) exhibits already some imperfections and disturbances as deduced from the somewhat more diffuse LEED reflexes and the slightly enhanced background. Once the films were prepared at 825 K, annealing at lower or higher temperatures did not improve the structural quality.

3.3.2.2 The structure of the co-deposited films (AES)

Figure 3.5 shows a series of AES survey spectra of the co-deposition series as observed by AES [co-deposition involved evaporating Al in 5×10^{-7} mbar oxygen in 10 minutes episodes]. Unlike the stepwise deposition method, the Al-LVV signal at 56 eV, (characteristic of Al^{3+} species)[7] is maintained throughout the deposition process up to film

thicknesses d of about 30 Å, estimated from values of the inelastic mean free path (IMFP) of the Auger electrons in Al_2O_3, taking the IMFP of the 489 eV Auger electrons in Al_2O_3 to be 13 Å[79,81,82]. The 489 eV peak was selected for Al_2O_3 thickness estimation because its intensity declined linearly with increasing Al deposition (see fig. 3.6)

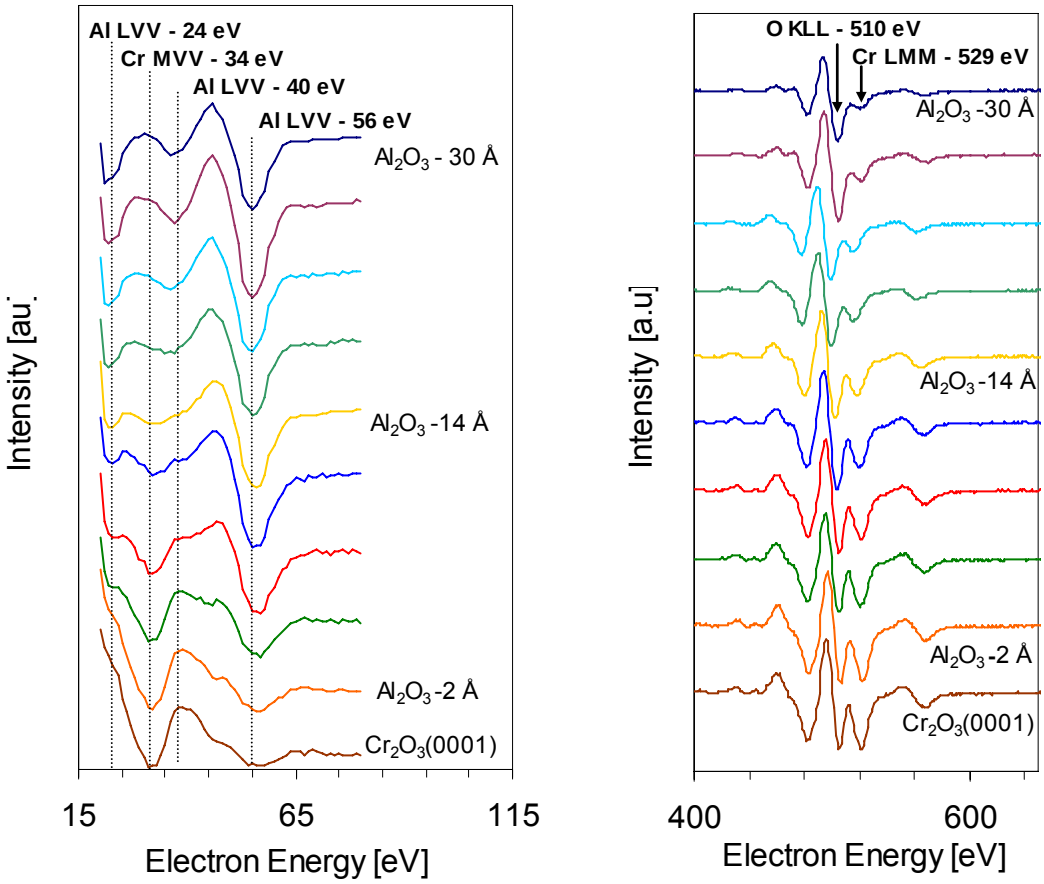

Figure 3.5 AE spectra of the co-deposition series taken for two energy regions: the left section (15-75 eV) and right (400-650 eV). All spectra were recorded at 2.5 kV primary beam energy.

In the series on the right from figure 3.5, one can clearly observe a gradual decrease of the Cr LMM Auger signals at 489, 529 and 571 eV with increasing Al_2O_3 coverage and a simultaneous appearance and rise in the Al LVV AES transition at 56 eV (left series). Remember that the 56 eV signal arises from the downshift of the metallic Al signal on the kinetic energy scale upon oxidation due to charge redistribution. At a thickness of about 14 Å (curve corresponding to ~ one Al_2O_3 unit cell)[7], the very surface-sensitive Cr MNN transition at 34 eV has disappeared completely. This would suggest that Cr is no longer present in the top-most layer. A few clues can be obtained from a closer look at the low

energy region. The spectra comprise mainly the Al^{3+} signal at 56 eV. This signal grows with increasing alumina coverage but stagnates at some point whilst a new one around 38 eV suddenly appears and starts to grow in intensity. Up to a coverage of about 30 Å (twelve oxygen and six Al layers, ca. two Al_2O_3 unit cells), the quasi-hexagonal structure of the substrate was maintained as deduced from the features of the LEED patterns as already pointed out in the previous section. The thicker the films (above 30 Å), the poorer were the quality of the corresponding LEED patterns, suggesting the onset of polycrystalline non-epitactic growth.

The thickness of the Al_2O_3 films were estimated from plots of calculated and experimentally determined IMFP values of Auger electrons in alumina as a function of the attenuation of the substrate Auger signals with increasing alumina thickness. The plots are shown in figure 3.6.

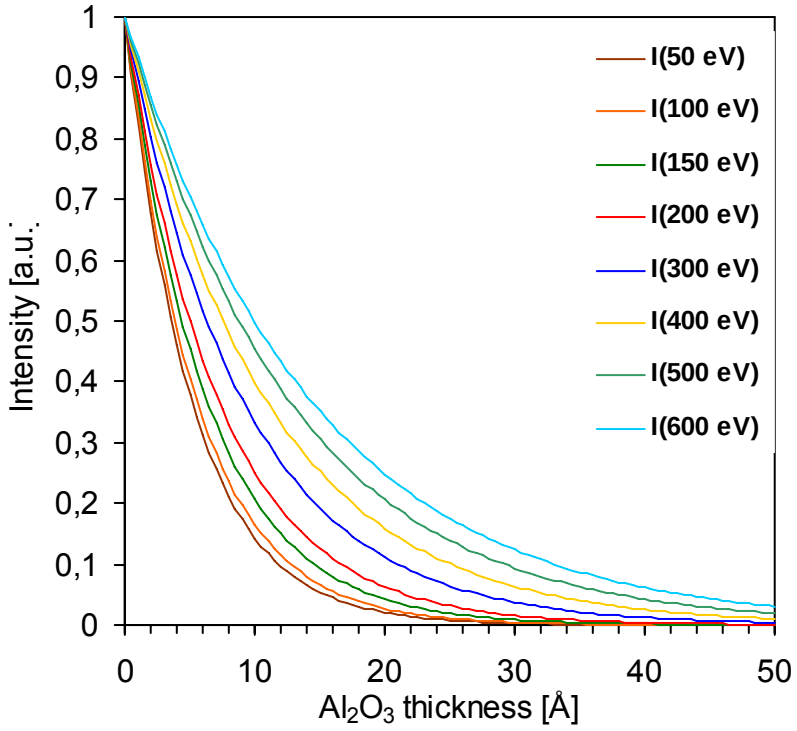

Figure 3.6: Plots of intensity (substrate) versus Al_2O_3 thickness for various Auger electrons estimated from calculated IMFP values of Auger electrons in Al_2O_3.

In figure 3.7, the intensities of the various species were estimated using the height of the respective Auger transitions. From the figure, one can say that within the limits of

experimental error, the intensity of the oxygen (O-KLL) transition at 510 eV is constant. This is particularly important because our substrate itself is an oxide. A significant variation would have indicated an unstable oxygen environment either in the substrate or adsorbate both of which are oxides. Also there is a near linear fall in the intensity of all Cr signals especially the 489 eV transition. The Al Auger electron intensity tends to increase sharply at first and then takes a normal but steady and linear increase with time. The surface sensitive Cr Auger electron at 34 eV also fell steadily at first, and then sharply after 30 minutes and disappears completely after 60 minutes. This behavior has been observed by several other workers who have investigated thin film growth with AES and have concluded that this sharp fall in the intensity of the substrate actually coincides with the completion of a full monolayer of the overlying species. This behavior agrees very well with an observation we made for the same series of measurements using ion scattering which indicated that chromium was no longer present in the first layer.

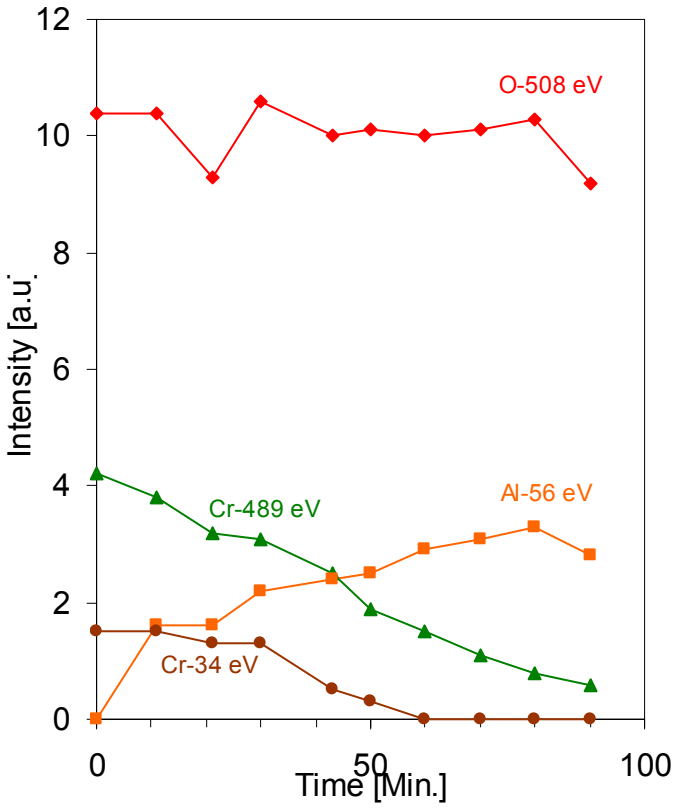

Figure 3.7: Intensity versus time plot of the most prominent Auger transitions observed during the co-deposition experiments. The intensities were estimated from the vertical peak to peak heights of the respective signals.

3.3.2.3 The composition and growth of the Al_2O_3 films (XPS)

For technical reasons, x-ray photoelectron spectroscopy measurements were carried out in a different chamber, and care was taken to reproduce the deposition conditions in this chamber as best as possible. We mentioned in the foregoing AES section that specific kinetic energy shifts of the Al signals monitor the stage of Al oxidation; i.e., chemical state identification was (at least to some extent) possible from AES data. However, XPS is by far a superior (and most utilised) method to monitor and identify valence or chemical state in surface chemistry. In heterogeneous catalysis, XPS is almost indispensable for this purpose.

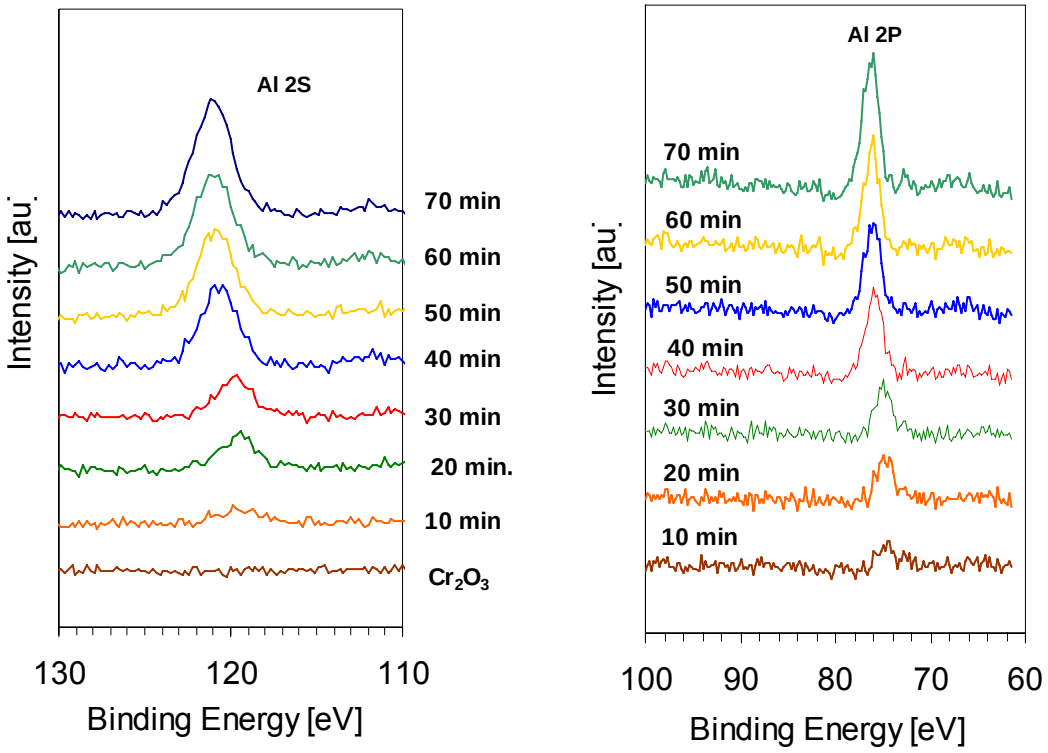

Figure 3.8: XP spectra of the co-deposition series: left-Al 2s and right-Al 2p regions. All spectra were measured with Mg k_α (1253.6 eV) radiation at 45° incidence and 0° exit angles. Note that the series on the left contain one spectrum in excess. This is because the 2p series are difference spectra, i.e., the substrate spectrum was subtracted from the spectra of each deposition episode.

An excellent example is provided by the work of Ertl and Thiele[83], who investigated industrial ammonia synthesis catalysed by Fe_2O_3 and found that the energetic positions of

the iron $2P_{3/2}$ level depended sensitively upon whether the catalyst species was reduced (706.9 eV) or oxidised (711.4 eV).

In Figure 3.8, we present XP spectra of our samples in the course of co-deposition of Al and oxygen. In detail, the Al 2s (left) and 2p (right) levels are monitored. The procedure was as follows: First, we recorded a survey spectrum; thereafter better resolved spectra were taken focusing on the Al 2s and 2p photoelectrons. The Cr 3p and O 2s regions were also recorded (see figure 3.9). As expected, the Al 2p and 2s peaks grow with increasing Al_2O_3 coverage whilst the Cr 3p peak decreases. The O 2s photoelectron peak intensity remains relatively constant. After 70 minutes and a total oxygen exposure of about 2000 L, the thickness of the Al_2O_3 film was estimated to be 13 Å. This value compares well with the one obtained from AES; we recall that under these conditions, the Cr LMM Auger transition at 34 eV could no longer be detected.

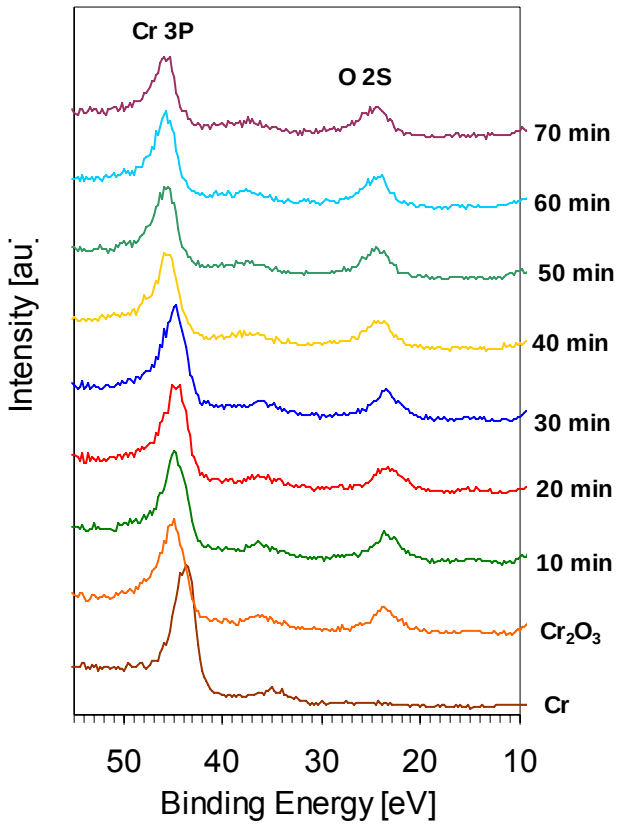

Figure 3.9: XP spectra of the co-deposition series showing the Cr 3p and O 2s regions. The series begins with metallic Cr, then its oxide, and finally 10 minutes episodes of Al_2O_3 deposition at 825 K.

The respective conclusions are also confirmed by the corresponding (see sec. 3.2.3) LEIS data. At this Al_2O_3 coverage and even prior to it, Cr is no longer detectable and therefore we conclude that it has to be absent in the topmost layer(s) and as a result, the LEED patterns we saw at coverages between 13 and 30 Å could not have arisen from the substrate.

For closer scrutiny, the Al 2s, 2p and O 1s peaks of the adsorbed Al_2O_3 film and the O 1s signal of the clean Cr_2O_3 substrate were fitted after Shirley background subtraction[26].

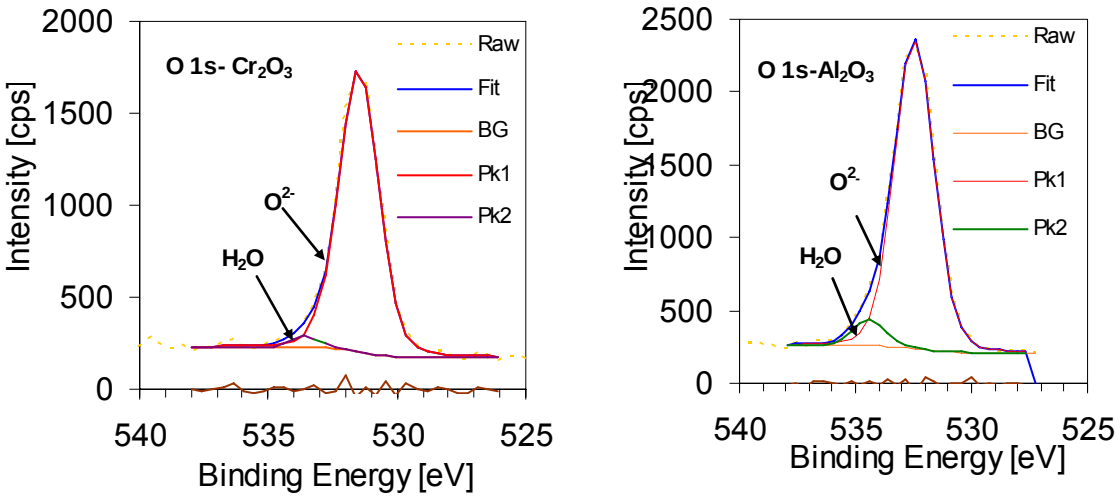

Figure 3.10: Fitted O 1s regions of Cr_2O_3 (left) and a 13 Å thick Al_2O_3 film (right) showing the presence of OH species at higher BE values in both cases. The fits were performed using the XPSPEAK package of R. Kwork[84].

All peaks were deconvoluted by a nearly symmetrical and mixed Gaussian/Lorenzian type of curve shape using the fitting package from XPSPEAK[84]. The fit parameters (FWHM, S.O.S, % Gauss/Laurentzian, type of background, etc.) were held constant throughout the study. The fitted peaks are shown in Fig. 3.10 (O 1s) and 3.11 (Al 2s, 2p) respectively. In the former, the O 1s region of the 13 Å thick Al_2O_3 film (right) and the clean Cr_2O_3 substrate (left) are presented. The fits show a small but relatively significant structure at 533.5 eV for Cr_2O_3 and 534.5 for Al_2O_3. These features, which are characteristic of oxides have been observed in many photoemission investigations of oxide surfaces and have been identified as water or OH species. The Al 2p and 2s regions (fig. 3.11) reveal only trivalent Al at binding energies of 75.8 and 120 eV respectively. From these observations, we

conclude that the films are completely oxidised. There is a broad shoulder around 80 eV in Al 2p region. Whether this peak belongs to Cr 3p or is due to final state effects is unclear.

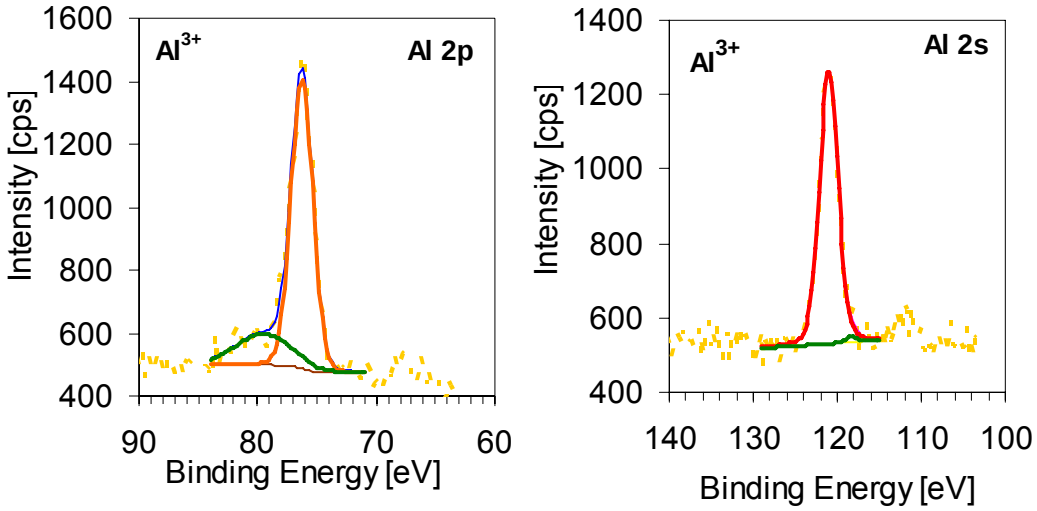

Figure 3.11: Fitted Al 2s and 2p regions of a 13 Å thick Al_2O_3 film.

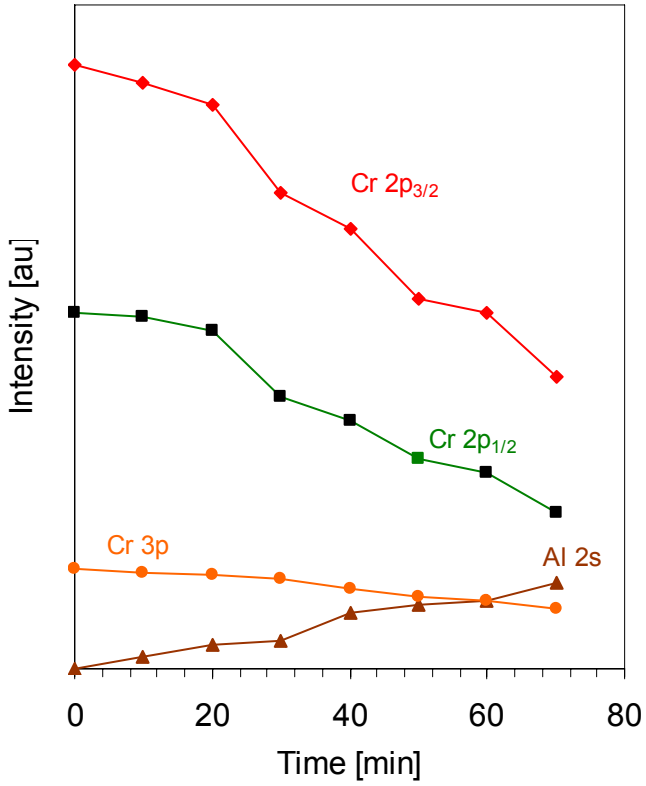

Figure 3.12: Intensity plots of the various photoelectrons as a function of aluminium deposition time. The intensities were estimated from the area under the respective curves after background subtraction (Shirley).

Figure (3.12) shows the changes in intensities of the various photoelectrons from the underlying Cr_2O_3 and the overlying Al_2O_3 as monitored by XPS.

The intensities were estimated from the area under the respective curves after Shirley background subtraction from the raw data. The intensity of the Cr 2p photoelectrons fall sharper than the 3p ones, which is not unexpected for the escape depths of these electrons are different. We also see a gradual but linear pattern in the trend followed by the Al 2s photoelectron.

3.3.2.4 Low-energy ion scattering spectroscopy (LEIS)

In many experiments involving thin and ultra-thin film growth, low energy ion scattering (LEIS) has been successfully exploited to gather information on the chemical composition of the topmost layer of the sample because it is extremely surface-sensitive.

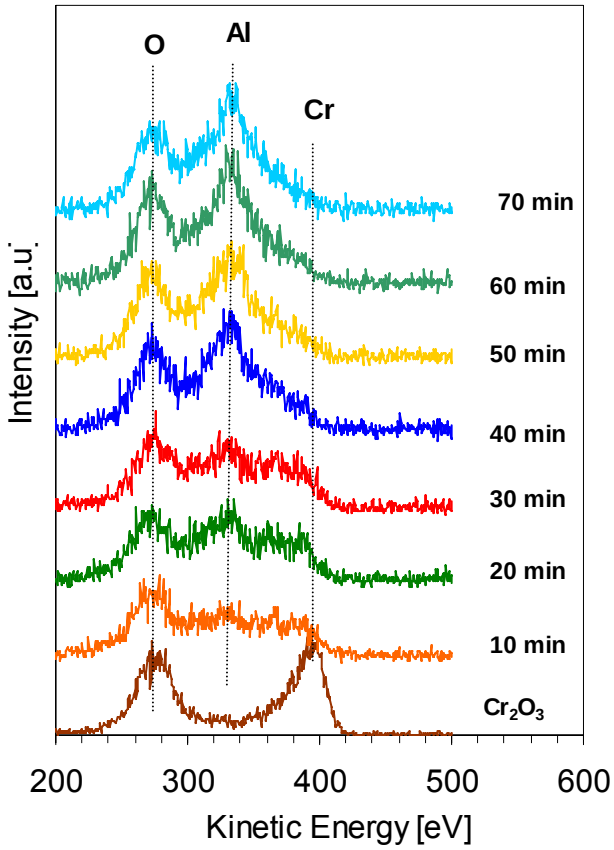

Figure 3.13: LEI spectra of the co-deposited films taken along side the XP spectra for each deposition episode. The spectra were recorded at beam energy of 0.5 keV and He partial pressure of $2 \cdot 10^{-7}$ mbar.

When combined with XPS, a fairly comprehensive judgment on both surface composition and chemical valence state of the surface region is possible. Shown in figure 3.13 are the LEIS spectra of the co-deposition series. It is clearly evident from the figure that even in the sub-monolayer regime; the deposition of ultra thin films of alumina causes an almost complete attenuation of the chromium LEIS signal. Clearly, at this stage, the deposit consists merely of a mixture of Al and O atoms, which is nevertheless dense enough to almost completely screen the Cr_2O_3 substrate. During the second and third deposition runs, this situation does not change proportionally, in particular with respect to the attenuated (but still visible) Cr signal, while the Al signal intensity increases gradually. One could perhaps invoke Cr cation exchange or diffusion to the surface to explain this behavior. However, as the Al + O coverage reaches an average thickness of about 8 Å (spectrum corresponding to 40 min deposition), the Cr signal disappears in the tail of the Al peak indicating that a limiting thickness beyond which Cr diffusion can no longer be effective may have been formed. At our deposition rate, this corresponds to a deposition time of 40 minutes. Above this coverage, Cr was no longer detectable in the LEI spectra. A broad shoulder at 385 eV may have arisen from multiple ion scattering effects, but certainly does not indicate the presence of Cr in the surface; Note that LEIS is not sensitive to changes in electronic state and as such does not lead to shifts on the energy scale as they may occur in AES and/or XPS. The uppermost spectrum of fig. 3.13 is believed to represent approximately a single layer of genuine Al_2O_3 (thickness ~ 13 Å).

3.3.3 Short Summary of results on the thin oxide preparation

We have seen in the preceding section that several factors play very important roles in the preparation of thin oxide films in UHV namely, temperature, cleanliness of the deposition source and state of the UHV chamber, nature of the substrate and adsorbate and most importantly, the method of choice. Because of the oxidic nature of our substrate, the step-wise deposition method failed to produce the desired results for obvious reasons. Al being a very electropositive metal has a very high affinity (molecular as well as atomic) for oxygen and as a result would attack any substrate with an oxidic character. We know from literature that the step-wise deposition method of preparing thin alumina films has been

successfully applied on single crystal metal surfaces in UHV, e.g., the Ta(110) surface[7]. That an aluminothermic reaction occurs between Al and Cr_2O_3 under real conditions is well known. A similar reaction at the microscopic scale is, as far as we know, unknown.

The co-deposition method yielded the desired results, i.e., well-ordered, epitactic thin Al_2O_3(0001) films. We used LEED as a qualitative tool only in our investigations because quantitative analysis using LEED-IV analysis for complex systems such as oxides is extremely demanding and unreliable.

We are convinced from the overwhelming spectroscopic and circumstantial evidence we have presented that the thin films are those of well-ordered Al_2O_3(0001) orientation probably with the α-geometry.

.

3.4 The Complex $Mo(C_3H_5)_4$

3.4.1 Synthesis

$Mo(allyl)_4$ is a very air and moisture-sensitive compound; so that its synthesis and handling were carried out under argon by using Schlenk or glovebox techniques. All solvents were freshly distilled from standard drying agents and thoroughly degassed under argon before use. The synthesis was carried out according to published procedures[85,86] which were modified in an attempt to improve on the yield.

4.5 g of Mg turnings were transferred into a clean, flamed and evacuated 250 ml three-necked round-bottomed flask under Argon. 50 ml of freshly distilled ether were added. The flask was cooled in an ice-bath and stirred until the mixture attained the required temperature. 1.7 ml of allylchloride (C_3H_5Cl) were diluted with 10 ml of freshly distilled ether and then added drop-wise to the Mg suspension through a septum. A milky suspension formed gradually. The reaction was complete after stirring under reflux for 3 h and the flask was cooled down to -35 °C. Whilst the flask was cooling down, 1.5 g of $MoCl_5$ were filled up in a 200 ml flask in a glove box and dissolved in 100 ml of freshly distilled ether. The dark brown solution was slowly dropped to the cooled flask containing the Grignard suspension through a septum. The reaction mixture was stirred at -35 °C for 2 h and then cooled down to -78 °C and left overnight. After 20 h of stirring at this temperature, ether was removed under vacuum. The solid residue was washed with two 50 ml portions of freshly distilled pentane. A yellowish-green solution was obtained. After removing pentane, the yellowish-green solid was stored under nitrogen at -20 °C.
The reaction equations are:

$$C_3H_5Cl_{(l)} + Mg_{(s)}(\text{excess}) \xrightarrow[\text{ether}]{0\ ^\circ C,\ 2\ h} C_3H_5MgCl \qquad (3.2)$$

$$C_3H_5MgCl + MoCl_5(l) \xrightarrow[\text{ether}]{-35\ ^\circ C,\ 1.5\ h} \xrightarrow[\text{ether}]{-78\ ^\circ C,\ 20\ h} \xrightarrow[-30\ ^\circ C]{\text{pentane}} Mo(C_3H_5)_4 \qquad (3.3)$$

3.4.2 Nuclear magnetic resonance spectroscopy (NMR)

In this section, we used mainly proton and carbon-13 NMR in liquid and solid phases to investigate the complex.

3.4.2.1 Proton (^{1}H) NMR (liquid and solid)

The liquid state proton and carbon NMR 1D spectra were recorded on a Bruker AMX 500 NMR spectrometer at room temperature at a magnetic field of 11.7 T, i.e. at resonance frequencies of 500.0 MHz for ^{1}H and 125.7 MHz for ^{13}C. Pentane d_{12} used to dissolve the complex for NMR analysis was distilled before use and thoroughly degassed during four freezing, thawing, and degassing cycles. The NMR samples were prepared in teflon-stoppered NMR tubes. A deuterated solvent was used for deuterium-locking. For chemical shift calibration of the NMR spectra, TMS was employed as external standard. The results obtained for the ^{1}H NMR of the complex in solution are presented below:

All solid state NMR measurements were performed at room temperature on a Varian InfinityPlus NMR spectrometer operating at a field of 14 T. Resonance frequencies are 599.97 MHz for ^{1}H and 150.87 MHz for ^{13}C. For all experiments, an MAS-probe was employed (Chemagnetics 4 mm). The powdered samples were packed under Ar atmosphere into zirconium oxide rotors in a glove box. For MAS experiments, the sample spinning frequency was adjusted in the range of 4 to 15 kHz, respectively, and was stabilised to ca. ±2 Hz. Typical $\pi/2$ pulse lengths were 3.4 μsec for the ^{1}H channel. For the MAS-spectra, the CPMAS technique[40] was combined with a rotor synchronised Hahn echo[28], which eliminates the dead time of the probe. Residual ^{1}HX dipolar couplings were suppressed using TPPM decoupling[42] with a B1 field of 50 kHz. Ramped amplitude cross-polarisation (RAMP-CP)[43] was used to enhance the CP efficiency at higher spinning rates. For each FID between 1000 and 20000 scans were accumulated.

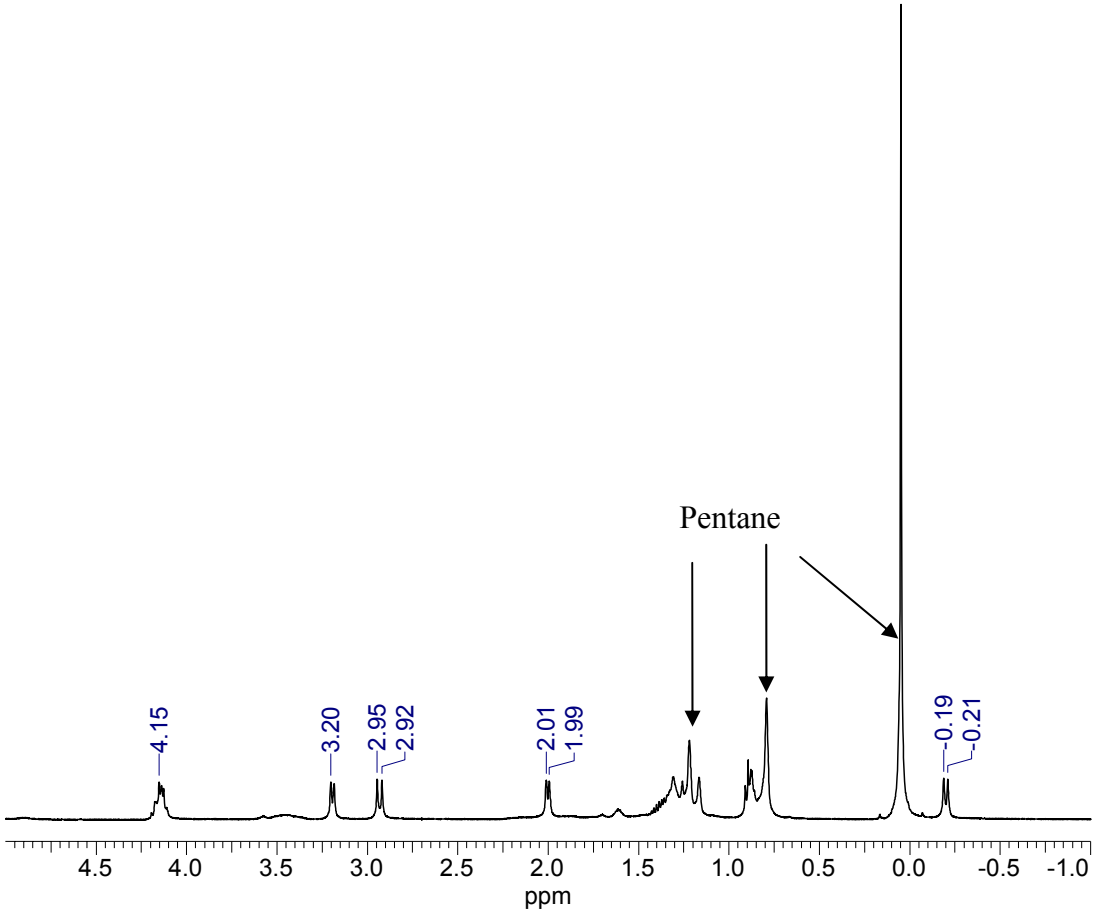

Figure 3.14: ^{1}H NMR spectrum of $Mo(C_3H_5)_4$ in pentane

The ^{1}H-NMR results we obtained for the complex in d_{12}-pentane showed five resonances (500.13 MHz, pentane-*d12*, 293 K; δ) -0,20 (H'_{anti}), 2.00 (H'_{syn}), 2.93 (H_{anti}), 3.20 (H_{syn}), 4.15 (H_x) in the ratio 1:1:1:1:1. The results compare excellently with literature[85,86].

The results obtained for the pure solid complex are as follows: 599.13 MHz, ^{1}H MAS, 293 K; δ) -0,31 (H'_{anti}), 0.99 (H'_{syn}), 1.97(H_{anti}), 3.11 (H_{syn}), 4.39 (H_x). The solid state spectrum compares well with the liquid state ^{1}H NMR spectrum, except that for the former, a small shoulder at 0.55 ppm is visible and is suspected of being caused by traces of water probably from solvents. This is probably the one disadvantage of solid state NMR in that peak broadening can sometimes minimise the predictability of the results. Also, the intensity relationship between the peaks is not as informatively important as in the liquid phase.

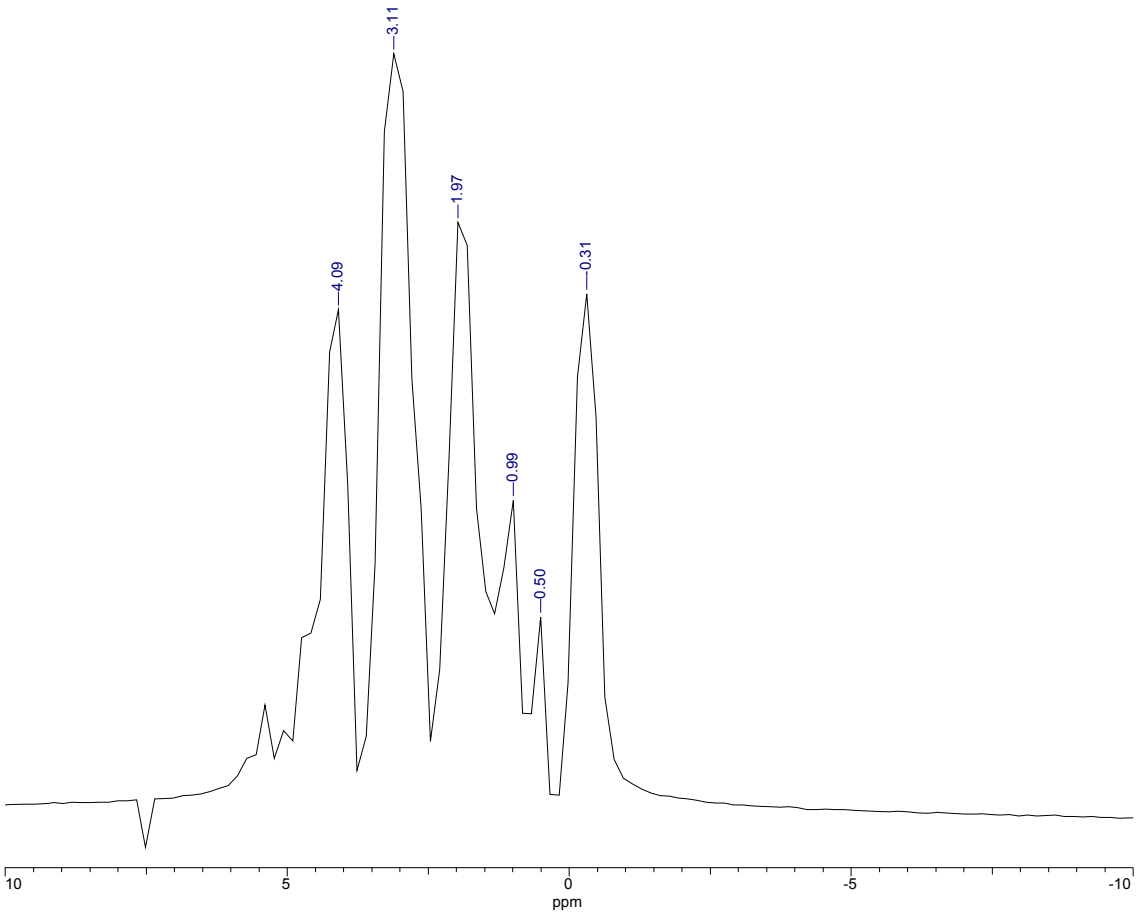

Figure 3.15: ^{1}H MAS spectrum of $Mo(C_3H_5)_4$

On the other hand, however, the absence of solvent contributions to the spectrum makes life very much easier. A combination of the two methods is therefore very useful for the proper assignment of resonances from a pure sample against those from solvents. This problem is normally solved by comparison of the solvent region to reference spectra of common solvents used in organic synthesis.

3.4.2.2 Carbon (^{13}C) NMR (liquid and solid phases)

The ^{13}C-NMR spectrum in figure 3.16 shows three distinct signals with a very smooth background. $^{13}C\{1H\}$ NMR (150.87 MHz, 293 K; δ): 105.71 (s), 68.82 (s), 41.22 (s). The one measured of the complex in solution (fig. 3.17) on a different spectrometer with a

different resolution also shows three distinct resonances at δ): 104.49 (s), 68.55 (s) and 50.75 (s). Except for the solvent region, again the results agree remarkably well.

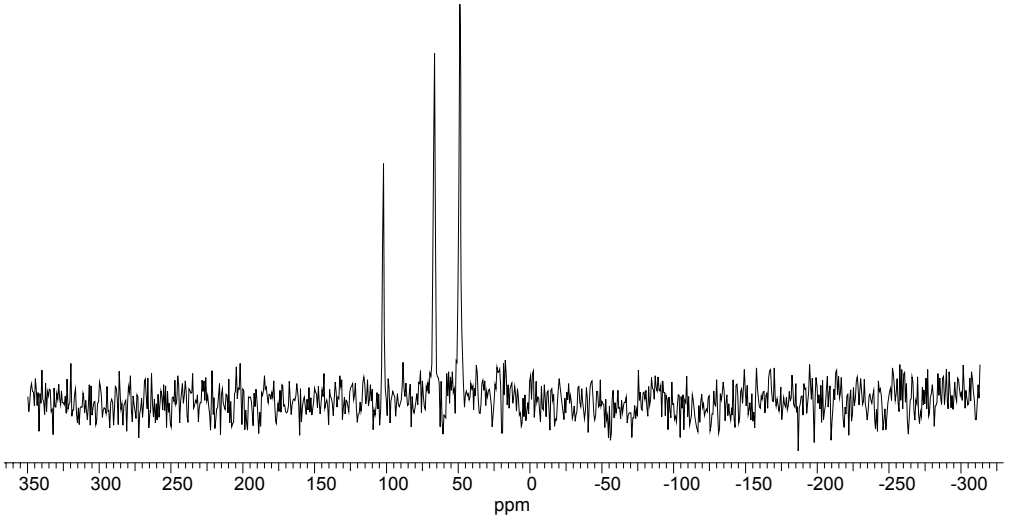

Figure 3.16: ^{13}C CP-MAS spectrum of $Mo(C_3H_5)_4$

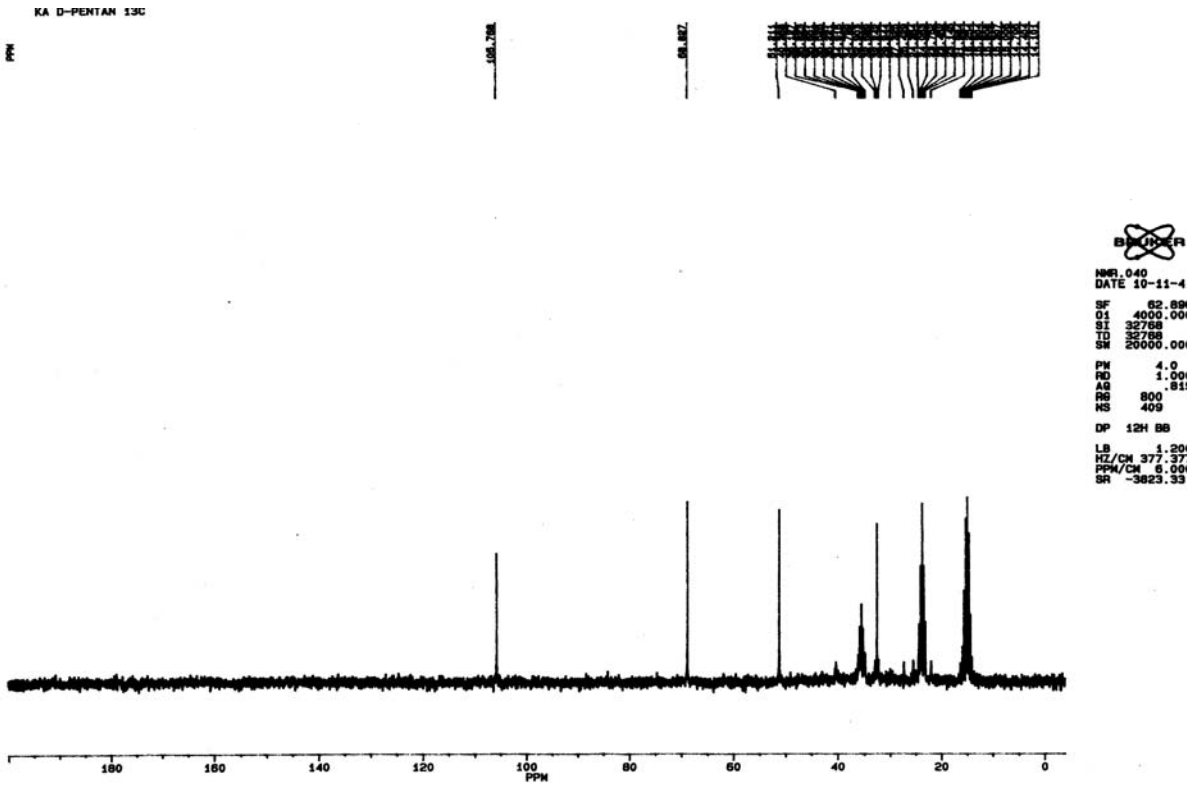

Figure 3.17: ^{13}C NMR spectrum of $Mo(C_3H_5)_4$ in pentane

These results further buttress the idea of four equivalent allyl groups and the chemically different environments of the terminal CH_2 groups.

To further investigate the bonding scenario in the M-C unit, the complex was gradually heated to two temperatures (413 and 443 K) and the corresponding products were monitored using ^{13}C NMR and the results are shown in the figure (3.18) below:

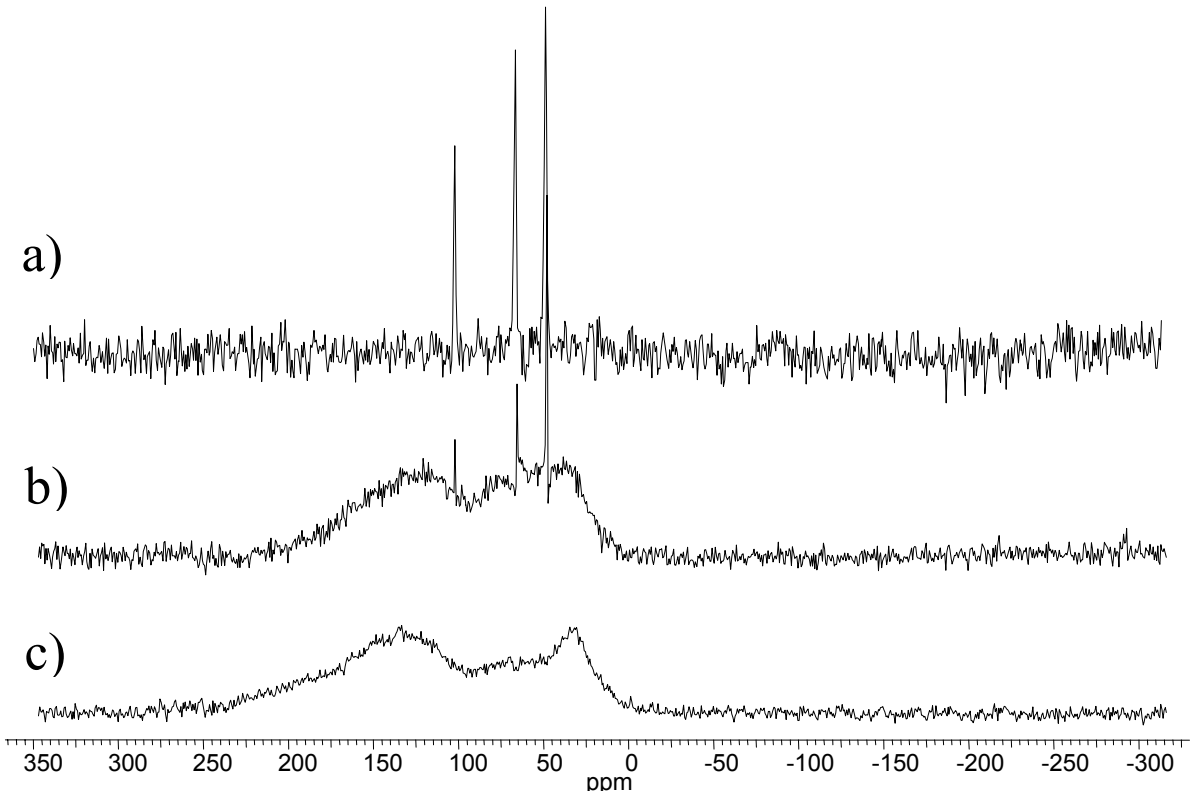

Figure 3.18: ^{13}C NMR spectra of $Mo(C_3H_5)_4$ at three different temperatures. a) depicts the intact complex at 300 K. b) middle spectrum represents the onset of decomposition at ~ 413 K whilst c) belongs to the completely decomposed species at T > 443 K.

These heating experiments were necessary to ascertain whether the complex is of the π, σ, or dynamic type. That the three peaks did not coalesce with increasing temperature is an indication that the complex is a symmetric π-allyl complex as is customary with transition metals. However, as the temperature was increased, we observed a decrease in the intensities of the three resonances and the onset of broadening. This phenomenon is the result of slow decomposition whereby the allyl ligands are slowly transformed into other

species, probably CO and Oxo species which could have arisen because the zirconium oxide rotor was no longer air-tight at such temperatures.

3.4.3 X-ray absorption fine structure (XAFS)

Mo K-edge was measured at the X1 beamline of HASYLAB (Hamburg, Germany). Throughout the XAS measurements, the double-crystal Si(311) monochromator was kept detuned at 60 % of maximum reflectivity to suppress harmonics in the x-ray beam. An ion chamber filled with pure nitrogen was used to monitor the intensity of the incoming beam. All data were acquired in fluorescence detection mode.

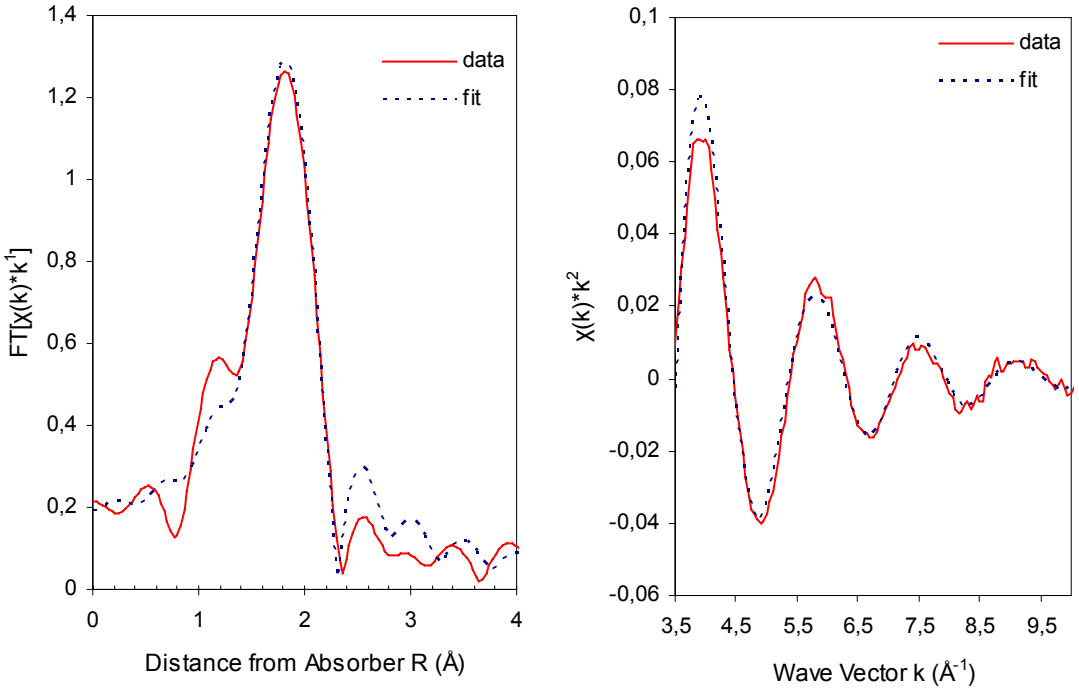

Figure 3.19: Results of the EXAFS analysis of a solution of $Mo(C_3H_5)_4$ in pentane.

5 ml of a solution of the Mo-allyl complex in pentane were transferred into a Teflon tube (45 mm long, 8 mm internal diameter and 1mm thick; 1.4 ml). Careful sealing with a stopper and adhesive tape in a glovebox prevented oxidation by air. The tube was attached to an L-shaped stainless steel piece with the aid of a transparent adhesive tape. The L-piece

was in turn attached to the goniometer and carefully aligned in the beam to maximise fluorescence signal intensity.

The synchrotron storage ring was operating in multi-bunch mode, with ring currents between 60 mA and 80 mA. Data acquisition times for one spectrum were between 30–45 minutes. IFEFFIT {8369}[87,88,] was used to fit scattering contributions based on theoretical scattering parameters obtained with the full multiple scattering code FEFF8.2 {8319}[87]. Data reduction (background removal and normalisation) was carried out with the HORAE package of B. Ravel[89].

The fits performed show good agreement between experimental data and theory. The left figure above presents the Fourier transformed EXAFS function of molybdenum tetraallyl (experimental and theory). The coordination number of 3.6 shows an average presence of 3-4 allyl ligands. The distance (2.35 Å) is an acceptable value and compares well with values found in the literature for similar compounds.

3.4.4 ICP-MS

EXAFS and NMR have both showed without doubt that the allyl complex was structurally intact, but the presence of other impurities like heavy metals can only be confirmed by a trace analytical method capable of detecting trace concentrations from the ppb to the ppt regimes. The presence of such impurities might lead to an eventual poisoning of the active site and therefore the catalyst. Because of availability, background knowledge and access to an ICP-MS instrument, and due to its choice as the tool in trace analysis, we decided to investigate the state of purity of the molybdenum complex using this method. Another deciding factor that required the use of ICP-MS was the need to confirm the presence or absence of silicon, which, as we shall see in the next section, turned out to be a great nuisance in our efforts to combine wet chemistry with UHV.

100 mg of $Mo(C_3H_5)_4$ were dissolved in 10 ml of freshly distilled pentane. From this, a 70 ppb solution was prepared by appropriate dilution in 50 ml of tri-distilled water using a volumetric bottle made of Teflon. Prior to analysis, a control run with tri-distilled water

was made in order to establish the background contaminants arising from the plasma torch. The sample was introduced in the plasma using a peristaltic pump coupled to the spectrometer. The sample flow rate was optimised for maximum intensity and signal to noise ratio.

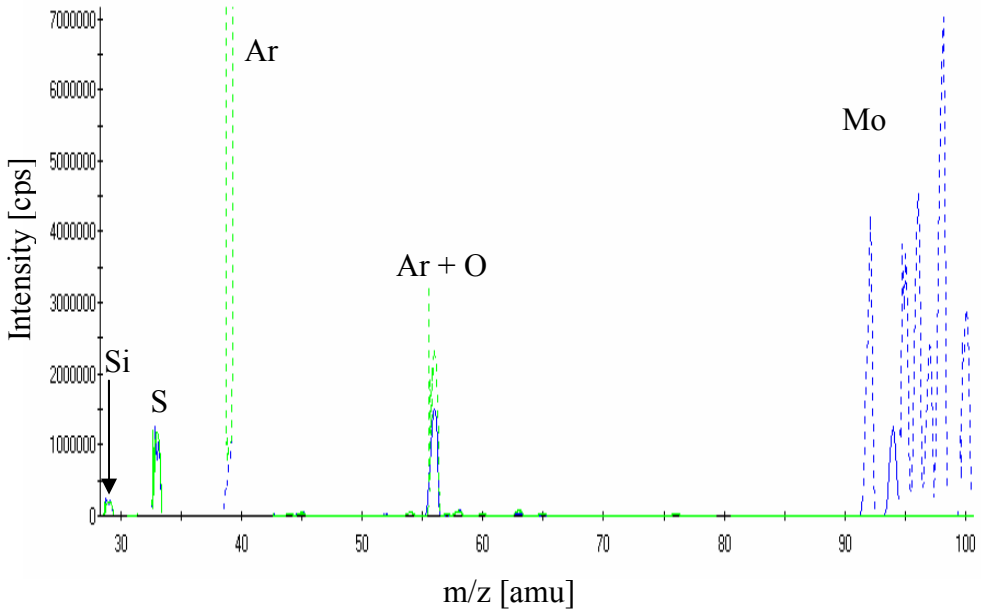

Figure 3.20: Survey ICP- Mass spectrum of a 70 ppb solution of $Mo(C_3H_5)_4$ in pentane.

Figure 3.20 shows the survey (m/z 0-100) ICP- mass spectrum of a very dilute (70 ppb) solution of the molybdenum complex in pentane. It is clearly visible from the spectrum that in the m/z range investigated, a very clean sample especially with regards to heavy metal contamination was evident. It should be borne in mind that the green line represents the control run, i.e., the result obtained with pure tri-distilled water.

The huge green peak at m/z value of 40 is due to argon, which functions both as plasma gas as well as coolant for the torch. The signal at mass 56 is an interference peak that is characteristic of an Ar and O unit (40 + 16). We know it is not due to iron because it is not possible to have such huge quantities of iron in tridistilled water. However, in ICP-MS setups with a better resolution, the iron peak should be much better resolvable from the Ar-O interference peak. The peak at m/z 32 is thought to arise from sulphur, a species that is always present in the plasma, whilst the one at 28 is due to silicon. The intensity of the

silicon peak is the same in both sample and tri-distilled water and therefore seems to be insignificant. But as we shall see later, silicon would turn out to be most significant adsorbate after wet chemical treatment of the thin oxide surface.

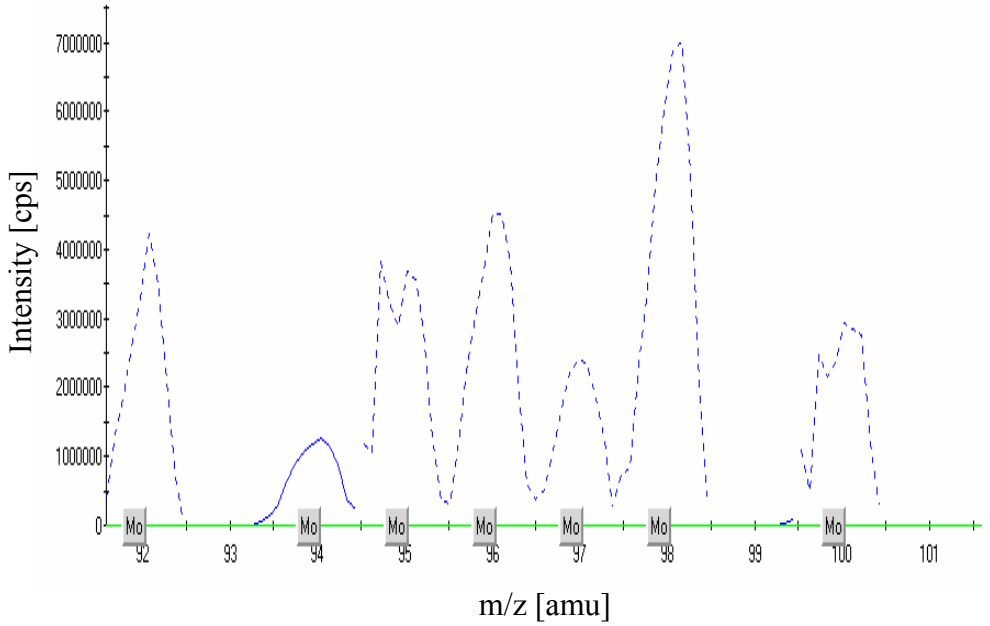

Fig. 3.21: ICP-Mass spectrum of the Mo region (92-100 amu) showing the relative isotopic abundance of the various Mo-isotopes.

In figure 3.21, the broken lines depict signals from the most abundant isotopes, while the solid line represents that of the least abundant. It is obvious from the spectrum that the isotopic distribution functions like a kind of finger print, because other elements such as zirconium also show up at similar m/z values but with a different isotopic distribution pattern.

3.4.5 Summary

We have prepared and characterised the tetraallyl complex of molybdenum and have shown with NMR, XAFS and ICP-MS methods that the complex prepared is the desired entity. The evidence from NMR is unquestionable and the supplementary information supplied by XAFS solidly buttresses the NMR findings, i.e., a bonding scenario between the central molybdenum atom and the surrounding allyl groups involving a π-overlap of orbitals. One

can therefore, accurately refer to the complex as the $Mo(\pi\text{-}C_3H_5)_4$. As far as our knowledge from the literature is concerned, this is the first time that XAFS and NMR studies of the pure complex in solution as well as in solid state, respectively, have been undertaken. The simple NMR spectra could only emanate from the π-complex containing only one molybdenum atom and four equivalent allyl groups. Because Mo easily forms multiple bonds with itself, sufficient cooling (-78 °C) during synthesis and workup phases was always necessary to avoid this reaction. An alternative product in the synthetic pathway is the $Mo_2(C_3H_5)_4$ complex. The compound contains a Mo-Mo bond and two bridging allyl units. This geometry would invoke at least three different allyl environments, a scenario that would lead to very complex proton NMR spectra that would be very difficult to explain. The evidence from ICP-MS points at a very clean and structurally intact complex.

3.5 The Substrate and Complex (Wet chemical reactions)

This section deals with the final stage of this work. Like in real catalysis, the combination of the active catalyst [$Mo(C_3H_5)_4$] and support (Al_2O_3) is a vital step in the whole process. Essentially, several methods exist for the deposition of a catalytically active species on top of the model support, but two main options are traditionally pursued, namely:

1) Straightforward evaporation of the metal/complex onto the substrate from a source in UHV or

2) Impregnation and exchange in solution. This procedure is less often pursued in surface chemistry because of the poor vacuum conditions that may result from the operation; it is however common in studies of electrochemically generated thin films[80].

Option (1) was not possible because heating destroys the complex between the melting point and evaporation temperatures. The less common method (2) was therefore pursued, because the sample was very much air- and moisture-sensitive, the exclusion of both species had to be ensured during the entire process.

The specially constructed wet chemical cell (see sec. 2.9.2.2) was flushed with argon at least one hour prior to the reaction. The Al_2O_3 (0001) surface was then flashed to 600 K in the UHV preparation chamber and cooled down before it was transferred to the high pressure compartment. At the same time, a standard solution of the complex in pentane was freshly prepared. A portion of the solution was introduced into the liquid reservoir of the high pressure cell through a septum using a carefully Ar-flushed syringe. The crystal was then turned 180° so that the Al_2O_3 surface now faced the top end of the transfer cell.

The main components of the transfer system have been thoroughly described in section 2.9.2 and would not be repeated here. After a routine transfer process, the pressure increase in the chamber is about two orders of magnitude. The results obtained are now presented below.

The reaction with alumina powder in real catalysis occurs as follows:

$$Mo(C_3H_5)_4 + [Al_2O_3](OH)_2 \xrightarrow{298\ K} [Al_2O_3][O_2]Mo(C_3H_5)_2 + 2C_2H_6 \quad (3.4)$$

3.5.1 $Al_2O_3/Mo(C_3H_5)_4$ (XPS)

We now present the first results obtained after wet chemical deposition of the complex onto the thin alumina surface from a solution of pentane.

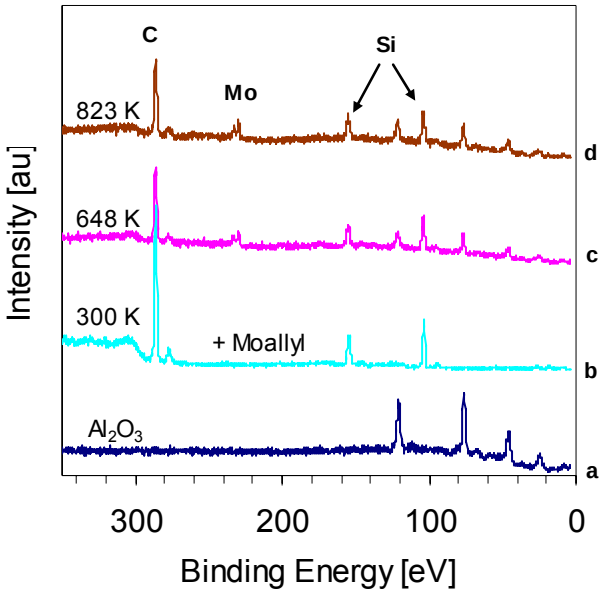

Figure 3.22: XP spectra of the first deposition series.

The bottom spectrum (a) is that of a thin (ca. 13 Å) alumina film grown epitaxially on chromium oxide. Its structure has been thoroughly investigated as reported in section 3.3.2, therefore we will not dwell much on that in this section. We see clearly that after the reaction (b), three new photoelectron peaks appear immediately at binding energy values of 103, 153 and 286 eV respectively. These peaks can be unambiguously assigned to the Si 2s, 2p and C 1s photoelectrons. Spectra (c) and (d) were obtained after (b) was annealed to the temperatures noted on the left of each spectrum. But why two new silicon peaks and no molybdenum signals were visible became the first question that needed to be answered.

3.5.2 Silicon contaminants

Because the stages involved from the synthesis to the wet chemical reaction are numerous and because several apparatus were involved, there was the need to screen every single stage for possible silicon contaminants. The results presented in the section below shall address this issue.

3.5.2.1 Control test with pentane (XPS)

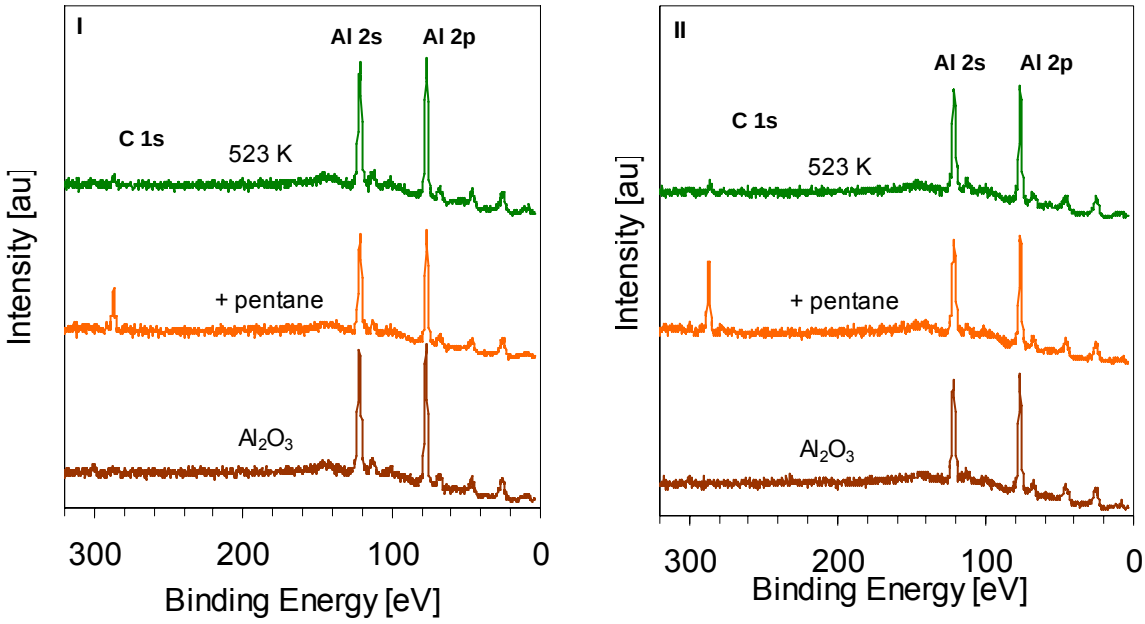

Figure 3.23: XP spectra of the control reaction with two portions of pentane that were pre-treated differently.

We therefore started with the two main solvents (pentane and ether) that were employed throughout the synthesis. By control test we mean repeating the wet chemical deposition using freshly distilled pentane and ether only.

The two series of XP spectra shown above portray two pentane portions that were pre-treated differently before being used in the wet chemical reactions with the thin alumina surface. Figure 3.23.I shows the series of spectra that were obtained after freshly distilled pentane was used, while 3.23.II shows the series of spectra obtained after freshly distilled

pentane was first transferred to a two-necked round bottomed flask and then connected to the Schlenk line that was used for synthesis as well as transfer purposes. The pentane sample was then flushed with argon for 20 minutes. This action was necessary because the complex sample was always handled in a similar way prior to each chemical deposition. That way, it was easy to check whether the silicon contamination was in fact from the Schlenk line since the valve system in the latter is normally greased with silicone based fats.

These reactions demonstrate not only the absence of silicon but also the weak physisorption of pentane on the oxide surface as is manifested by the appearance of a small C 1s peak around 286 eV. This peak was, however, completely removable upon heating, an indication that the carbon signal was not due to graphite, a species that desorbs only after sputtering and annealing to very high temperatures. There was therefore the need to continue to look further for other sources of silicon contamination.

3.5.2.2 Control tests with ether (XPS)

A similar control test as carried out for pentane above was repeated for a similar fraction of freshly distilled ether through which argon was flushed on a Schlenk line. In figure 3.24, the reactivity of ether towards the substrate is clearly evident from the huge C 1s peak (b), which, on comparison with the C 1s peak of the pentane series is very significant. This scenario is not unexpected as the polar nature of ether makes it very reactive when brought in contact with surfaces containing species that have a high affinity for oxygen. In this case, it could be reasonably assumed that a kind of weak bonding must have taken place between the oxygen atoms from diethyl ether and aluminium atoms from the surface. Also, oxygen atoms from Al_2O_3 may have also formed weak bonds with the hydrocarbon residue of the ether molecules. This weak coordination of ether to transition metal complexes has been frequently observed in x-ray crystal structure analysis of such complexes. But the most important result again is the absence of silicon. The need to search further became even more inevitable.

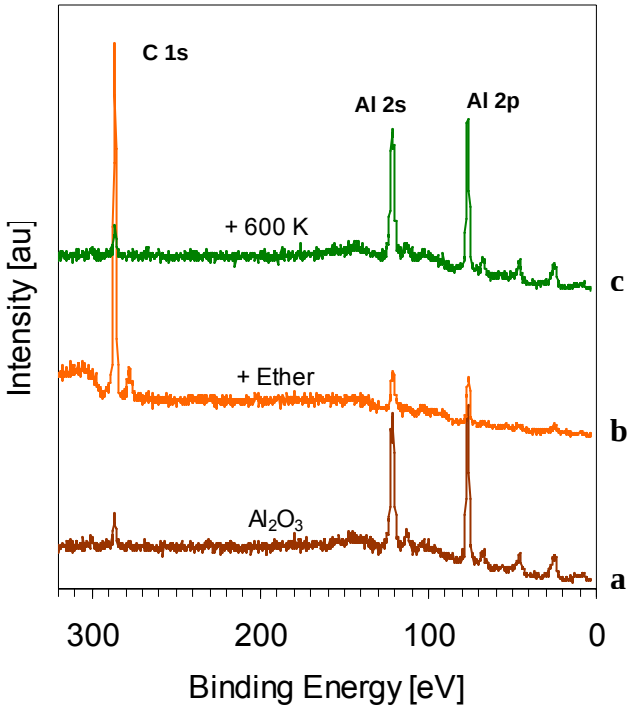

Figure 3.24: XP spectra of the control reaction using 5 ml of freshly distilled ether.

3.5.2.3 The Grignard Reagent (XPS)

The synthesis of the complex was done in two steps. It was therefore feasible that a source of silicon could be allyl chloride or its magnesium counterpart (see section 3.3.1). A freshly prepared Grignard solution was used. The suspension was allowed to settle down and a few milliliters of the clear ether portion was collected with a syringe and used as in section 3.5.1 The most striking feature of the results in figure 3.25 is the qualitative prowess of the XPS method. The various components of the Grignard solution, in this case allyl magnesium chloride (C_3H_5MgCl) are immediately visible at 52.5 eV (Mg 2p), 91.6 eV (Mg 2s), 200.28 eV (Cl 2p), 272.6 eV (Cl 2s) and 286.5 eV (C 1s), respectively. The combination of wet chemistry could therefore turn out to be as useful to the surface chemist as to the synthetic organic chemist. The presence of silicon in the educts can therefore be eliminated based on these results.

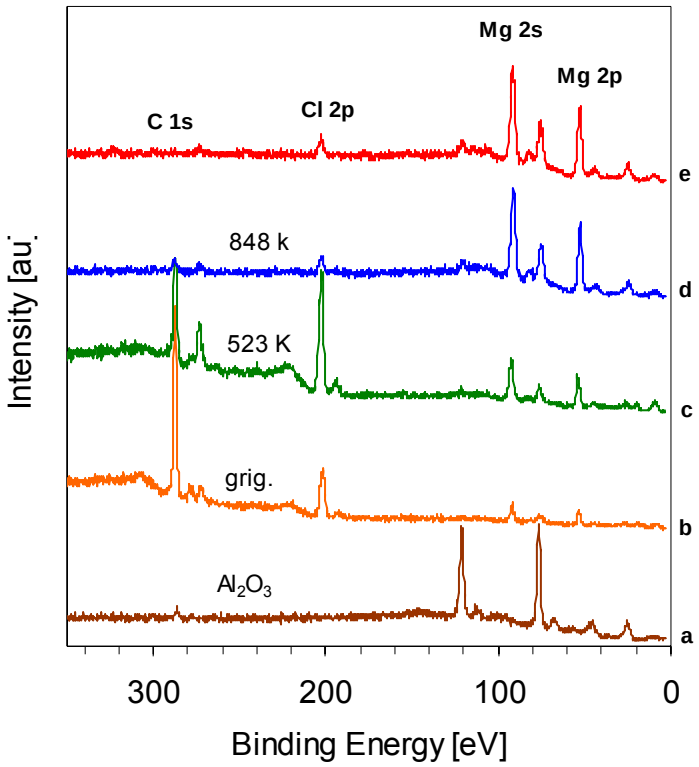

Figure 3.25: XP spectra of the Grignard portion after reaction with the surface.

3.5.2.4 The $MoCl_5$ Reagent (XPS)

$MoCl_5$ is available commercially and was therefore purchased for the synthesis. In the 5g bottle that was purchased, the concentration of silicon based impurities was estimated as being below 0.002 %. A dilute solution of the crude (as bought) sample was prepared in ether and tested. A 0.013 M solution of the sample in ether was prepared after careful sublimation of the crude chloride. A similar concentration was made from the crude sample. Both samples were tested with the aid of our wet chemical transfer system on the alumina surface under similar conditions.

A look at the left figure (crude sample) reveals the appearance of two huge silicon peaks alongside the chlorine, molybdenum and carbon photoelectron peaks. The figure on the right on the other hand shows only Mo and Cl signals. This was the first indication that if not all, part of the silicon contamination does evolve from the pentachloride.

A fresh synthesis was therefore carried out using freshly sublimated $MoCl_5$.

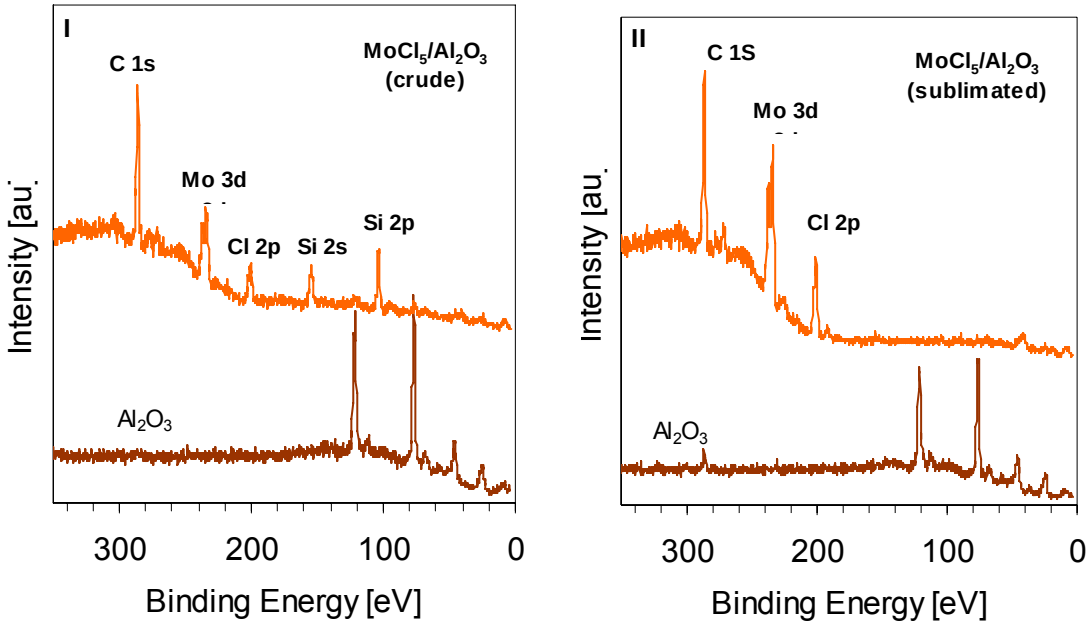

Figure 3.26: XP spectra of 0.013 M solutions of I) $MoCl_5$ tested crude (as bought) and II) after sublimation of the crude sample.

It seems reasonable to assume also that the presence of silicon hinders molybdenum uptake from solution as evident in the weaker Mo signal from the crude sample. The intensity ration of molybdenum in the crude sample to that in the refined one is almost ½. We already saw in section 3.5.1 that Al_2O_3 seems to show some kind of preference for silicon from a mixture of the silicon and molybdenum under the prevailing conditions during the wet chemical reactions. It could also be that the atomic sensitivity factor of molybdenum is compromised by the presence of silicon in the XPS experiments.

3.5.3 $Al_2O_3/Mo(C_3H_5)_4$ from freshly sublimated $MoCl_5$ (XPS)

After the apparently promising results presented from the control tests with pentane, ether and molybdenum pentachloride, we were encouraged to repeat the synthesis with freshly sublimated portions of $MoCl_5$ in a bid to rid our product of silicon contaminants. After NMR, and ICP-MS analysis of the complex, which indicated that the complex did not contain any significant amounts of silicon, we proceeded to the next stage, i.e., the wet

chemical deposition of the complex from solution. The results we obtained are presented in figure 3.27.

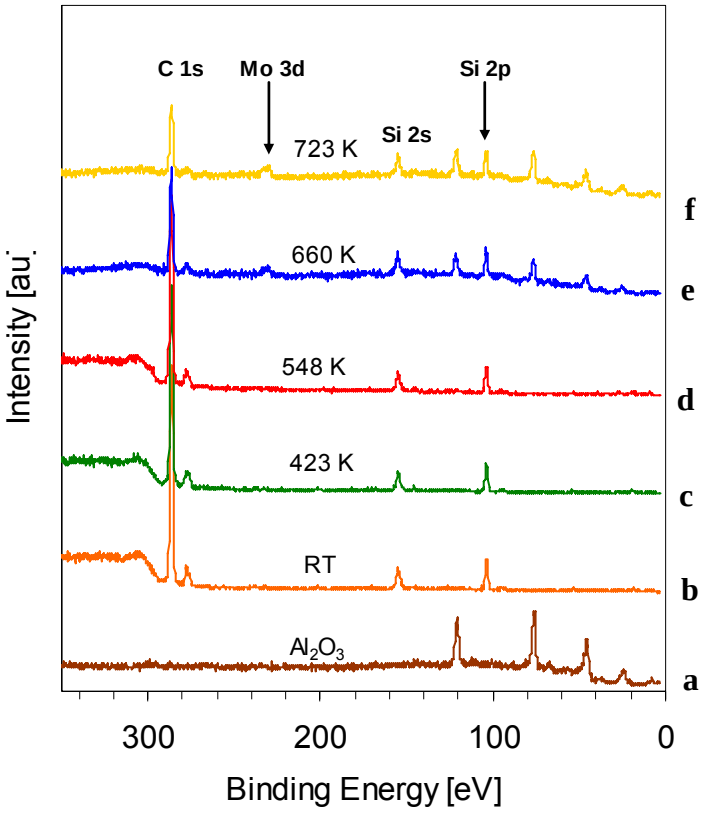

Figure 3.27: XP spectra taken after wet chemical deposition using freshly synthesised complex. The latter was prepared using freshly sublimated $MoCl_5$.

If we take a closer look at figure 3.27, several interesting revelations become clear. First, the silicon contamination which had been thought to be overcome has returned (b). Second, the molybdenum 3d photoelectron peak, which is the most intense signal in molybdenum compounds, does not appear immediately upon reaction with the surface (b, c, d). Rather, it becomes visible only after the crystal was annealed to higher temperatures (660 K in this case, (e)). This phenomenon was also observed for the first series of reactions presented in section 3.5.1). We also observed an intense C 1s peak at 286.3 eV, a binding energy value that is generally ascribable to hydrocarbons. Upon annealing, we observed a gradual decrease in the intensity of the C 1s signal, but no apparent shift in its position on the binding energy scale. This observation was made for temperatures as high as 723 K (f) and would suggest that no significant change in the chemical state of carbon has occurred.

3.5.4. $Cr/Cr_2O_3/Al_2O_3/Mo(C_3H_5)_4$ monitored by UPS

Hydrocarbon species adsorbed on clean metal surfaces are often cracked to pure carbon and consequently it was inferred from this experience that carbon species present above temperatures of 600 K may no longer belong to pure hydrocarbons.

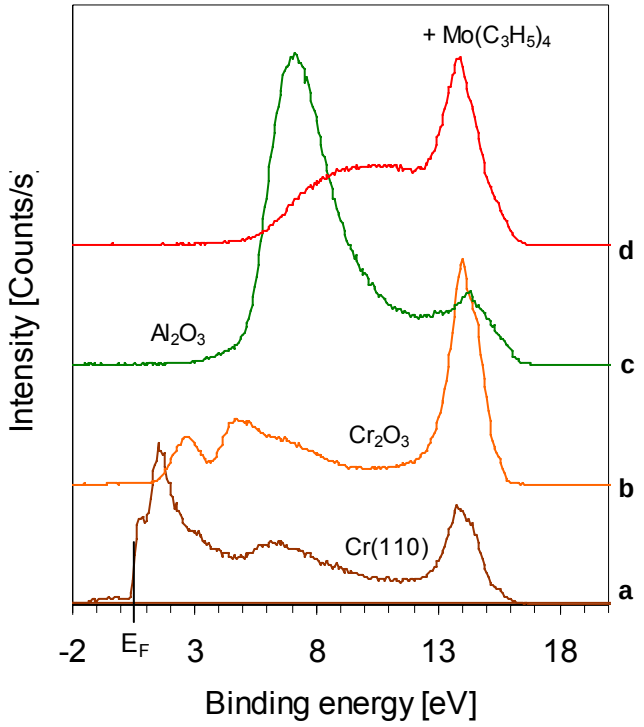

Figure 3.28: He I UP spectra showing the different stages involved from a single metal crystal surface to one loaded with $Mo(C_3H_5)_4$. All spectra were taken at a discharge current of 100 mA.

The need to use ultra violet photoelectron spectroscopy (UPS) to investigate the hydrocarbon unit especially at these high temperatures became necessary to attempt identification of the nature of our oxide/complex species in UHV. Furthermore, temperature-induced desorption of the fragments after wet chemical deposition and monitoring the fragmentation pattern with a mass spectrometer also became inevitable. It was assumed that if the species present on the surface at these high temperatures were indeed hydrocarbon units, more precisely allyl units, then it should be possible to observe mass 41 (C_3H_5) and related masses due to its fragmentation products and the electronic

density of states should be comparable to those of the allyl radical in the gaseous phase. The results presented in the following section shall be addressing this issue.

The spectra in figure 3.28 were collected with a SPECS UVS 10/35 He I discharge lamp. The bottom spectrum (a) is that of clean Cr(110) surface showing the typical transition metal 3d density of states between the Fermi level and binding energy value of 5 eV. The peak at 14 eV is due to secondary electrons. The spectrum of Cr_2O_3 (b) also agrees well with those from the literature[68,70,71]. The UP spectrum of a 15 Å thick alumina compares well with those of bulk alumina and thin films grown on Ag(110) and Ag(111) surfaces[90] (c). The huge peak at 7 eV with the shoulder at 10 eV is consistent with Al_2O_3 formation. The small peak around 13.5 eV is believed to be due to hydroxyl species. We would like to refresh your memory at this stage concerning the presence of OH species on the alumina surface. XPS results (sec. 3.3.2.3, fig. 3.10) also provided evidence for this behaviour. The broad peak of the uppermost spectrum (d) between 4 eV and 12 eV is believed to contain electronic density of states of the allyl radical[91,92,93].

From Literature, five peaks have been observed from theoretical and experimental investigations[94] of the gaseous allyl radical between binding energy values 0 - 4.97 eV. A comparison with our results, taking work function changes and charging effects into consideration would imply that the region covering the broad shoulder (4 – 12 eV) contains the electronic states of the molybdenum allyls.

3.5.4.1 $Al_2O_3/Mo(C_3H_5)_4$

A new deposition series was investigated using XPS and temperature induced desorption of the fragments using mass spectrometry. After the wet chemical deposition, the surface was investigated first with XPS and then annealed progressively in selected steps to higher temperatures as already mentioned.

3.5.4.2 $Al_2O_3/Mo(C_3H_5)_4$ (MS/TID)

As already mentioned in section 3.5.4.1, the existence of intense C 1s signals at temperatures as high as 800 K after wet chemical reactions needed further clarification as to whether the carbon species were due to graphitic carbon or hydrocarbons. The need to monitor the evolution of the hydrocarbon fragments at these high temperatures (> 600 K) became necessary.

The mass spectra were obtained during the heating process to the various temperatures listed in figure 3.29, which shows spectra taken of the residual gas (bottom) in the chamber and those taken after the sample was heated to the temperature indicated to the right of each spectrum in the series on the left. The crystal was heated to the desired temperature and maintained at this temperature for 15 minutes. During this period, mass spectra were recorded of the desorbing species. The mass spectrum with the most intense signals was selected for the particular temperature.

The usual pattern of H_2, H_2O, CO and CO_2 in the residual mass spectrum is evident. The absence of mass 32 is indicative of a leak-free vacuum. We observed the onset of desorption and or decomposition at 598 K (ca.13 mV, Ni/NiCr thermocouple). This temperature also marks the onset of desorption of hydrogen. At this temperature, masses 41 $(C_3H_5)^+$ and 42 (C_3H_6) appear whilst the intensity of the C 1s photoelectron followed by XPS falls significantly (fig. 3.29). The XP spectra were recorded after every heating episode with the sample at 300 K.

In addition, masses 56 (C_4H_8) and 58 (C_4H_{10}) appear at this temperature. Each time, there is a corresponding decrease in the C 1s intensity but no shift in its position and at the same time there is an enhancement of the substrate (Al 2s and 2p) photoelectron peaks (fig. 3.29). This trend would suggest a layer-by-layer desorption of the allyl species with temperature.

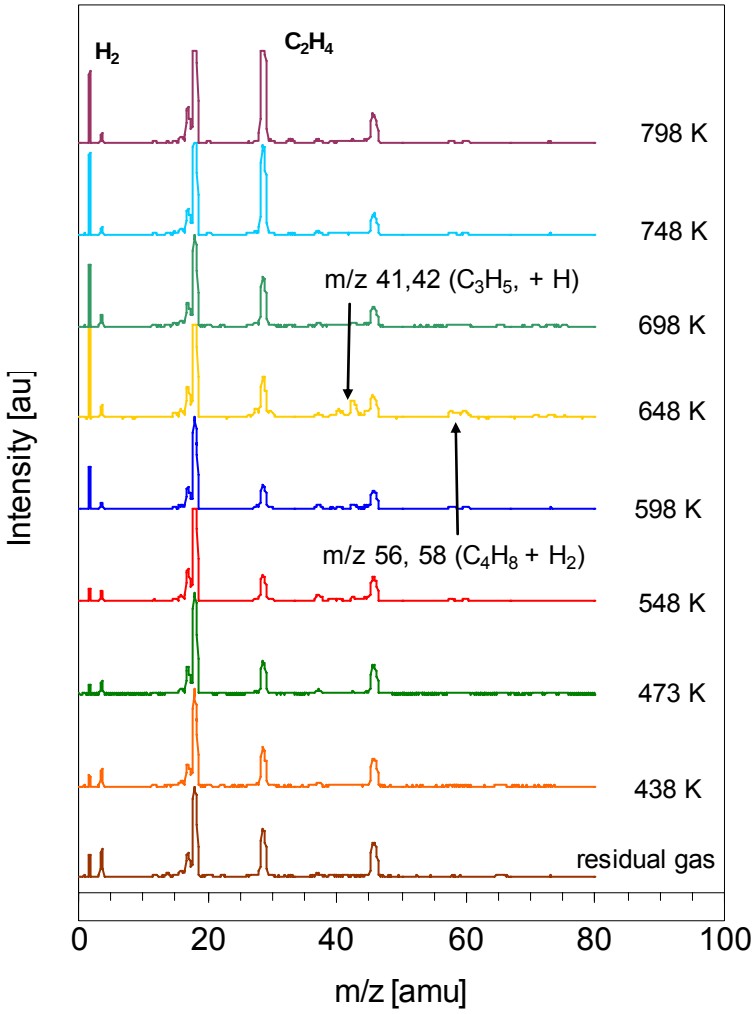

Figure 3.29: Mass spectra obtained after temperature induced desorption experiments.

At 648 K, m/z values of 41, 42, 56 and 58 peak off, whilst masses 2 (H_2) and 28 (C_2H_4) show a rapid increase in intensity.

In the XPS data, 648 K marks the appearance of the Mo 3d peak and more allyl desorption followed by further enhancement of the Al photoelectron peaks. That the mass 28 is due to ethene formation and not from carbon monoxide is supported by the lack of oxygen in the mass spectra. Up to the final annealing temperature of 798 K, significant amounts of hydrocarbon (C_2H_4) and molecular hydrogen desorption were observed.

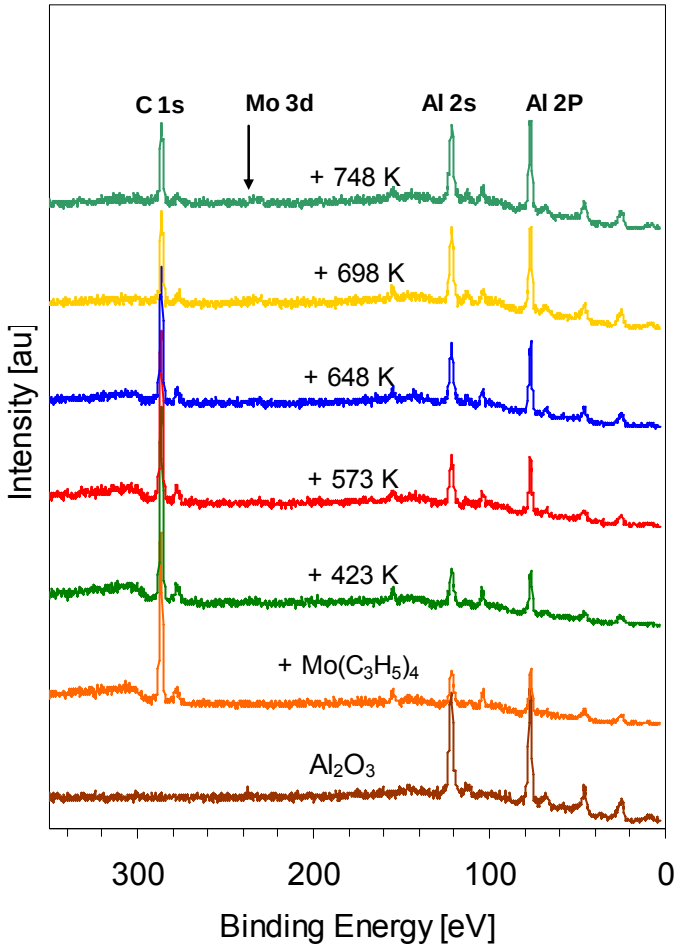

Figure 3.30: XP spectra obtained after every heating episode.

Again, the C 1s region in the corresponding XP spectra further supports the fact that even at these high temperatures, the desorbing species still arise from hydrocarbon units on the surface.

3.5.4.3 Short summary on wet chemical deposition experiments

In section 3.5, we have demonstrated the ability to combine UHV and wet chemistry. This is perhaps the most important achievement in this work and becomes even more important when one considers the chemistry of the compound involved in the process, namely, $Mo(C_3H_5)_4$. That it was possible to deposit the latter from solution on the surface of Al_2O_3 in a relatively intact form cannot be overemphasised. This is clearly demonstrated in

section 3.5.4.2. Another very important lesson that could be learned from these results is that of silicon contamination. Although we were in a position to pin-point one very important contributor to the contamination, we did not succeed in getting rid of silicon despite exploring all possibilities within our reach. Even though the concentration of silicon in the sample was comparable to that in tri-distilled water (see fig. 3.20), the Al_2O_3 surface shows a striking preference for silicon as against molybdenum and the results do not reflect in any way the relative concentrations of the two elements in solution. This preference for silicon by many chemical systems has long been recognised by biochemists and trace analysts to the extent that all work undertaken by such groups is done using glass-free apparatus. Repeating the synthesis in quartz glass (more resistant to chemical corrosion than normal glass) did not solve the problem either. It would therefore be reasonable to assume that the only significant contributor of silicon when using refined $MoCl_5$ is the glass ware due to silicon enrichment. This is particularly so because the second phase of the synthesis (see 3.4.1) involved lengthy (up to 20 h) stirring with a solution of $MoCl_5$, a compound that is known to posses some degree of corrosiveness towards a wide range of substances. The only alternative therefore is to replace glass with non-silicon based materials such as Teflon or borosilicate glass (very inert). This would include the Schlenk line, the transfer cell, relevant sections of the manipulator, etc.

.

3.6 Towards Catalysis

3.6.1 General comments

In the previous sections, we have been dealing with the synthesis and characterisation of the catalyst itself, but the ultimate goal would be the investigation of the catalytic activity of the prepared material using in-situ methods like XAFS. Since preparation of the catalyst (thin oxide, sysnthesis and wet chemical reactions) are carried out in a laboratory that is sometimes tens and even hundreds of kilometers away from the synchrotron source, there is the need to construct an XAFS and catalysis cell. This cell should be capable of storing the prepared surfaces under inert conditions and must withstand rigorous conditions during transportation to the light source. My project was part of a larger project whose main goal among others was to design such a portable XAFS cell. Because the main cell was not forthcoming at the time, we decided to construct a "rough" version of the former and tests using solutions of $Mo(allyl)_4$ on an $Al_2O_3(0001)$ single crystal surface showed that it is fully operational under the test conditions.

In order to carry out XAFS measurements using the cell, a solution of the complex in an evacuated and well stoppered flask was taken to a glove box together with the cell as shown in figure 2.26. The cell was then coupled up in the glove box. First the Teflon block and crystal were screwed in place, and then a few micro liters of the complex were dropped on the crystal surface and allowed to dry off. Finally, the hat was screwed in place (fig. 2.25) and the apparatus was mounted on the beam line on a goniometer. The two ridges (fig. 2.24) were used for fine alignment in the beam.

In order to test whether the cell was air and vacuum tight, we exploited the sensitivity of the allyl complex to air. After recording a spectrum of Mo K-edge using the closed cell, we removed the teflon hat and rescanned the surface under the same conditions. As expected, the second spectrum was visibly different from the first one, an indication that the allyl groups had undergone significant chemical transformation in air. In fact, we used this test to verify the structural integrity of all Mo-allyl samples we investigated using XAFS and it was from one such test that we found out that a sample sent to us from a different

laboratory had actually decomposed. It was based upon this experience that we decided to synthesise the Mo-allyl complex ourselves. The fluorescence spectrum of the Mo K-edge of the decomposed sample did not show any significant changes in the nature of the spectrum with and without exposure to air.

3.6.2 Preliminary metathesis tests at 300 K and propene partial pressure of $5 \cdot 10^{-7}$mbar

We performed preliminary tests on the catalyst after establishing the existence of Mo-C_3H_5 species on the surface of the single crystal as revealed by figures 3.29 and 3.30 respectively. Propene gas ($5 \cdot 10^{-7}$mbar) was fine-dosed through leak valves into the analysis chamber for 15 minutes at 300 K. The gas was shut off and the vacuum was allowed to recover for several hours. The crystal was heated gradually to higher temperatures while the desorbing species and fragments were monitored with a quadruple mass spectrometer. In figure 3.31, the spectra "residual gas" and "residual gas 2" depict the clean vacuum prior to propene dosage and that after propene dosage respectively. Traces of butene and butane (metathesis products of propene at 300 K) are already detectable in the mass spectrum "residual gas 2". The temperature range 423 K to 598 K did not produce any significant changes in the spectra. However, at 673 K, masses 2, 41, 42, 43, 56 and 58 appear to increase in intensity. The sample was maintained at 698 K for about half an hour, while the fragments were monitored with time. The intensities of masses 56 and 58 continued to grow with time, as well as those for masses 41 and 42. Significant hydrogen desorption was observed only after 17 minutes heating at 698 K. Mass 28 was almost completely suppressed, an indication that this fragment may not be present in the mixture under the prevailing conditions. This would hint at a selective metathesis in favour of butene.

These experiments would need to be revisited to complete this work, but the initial tests have shown promising results.

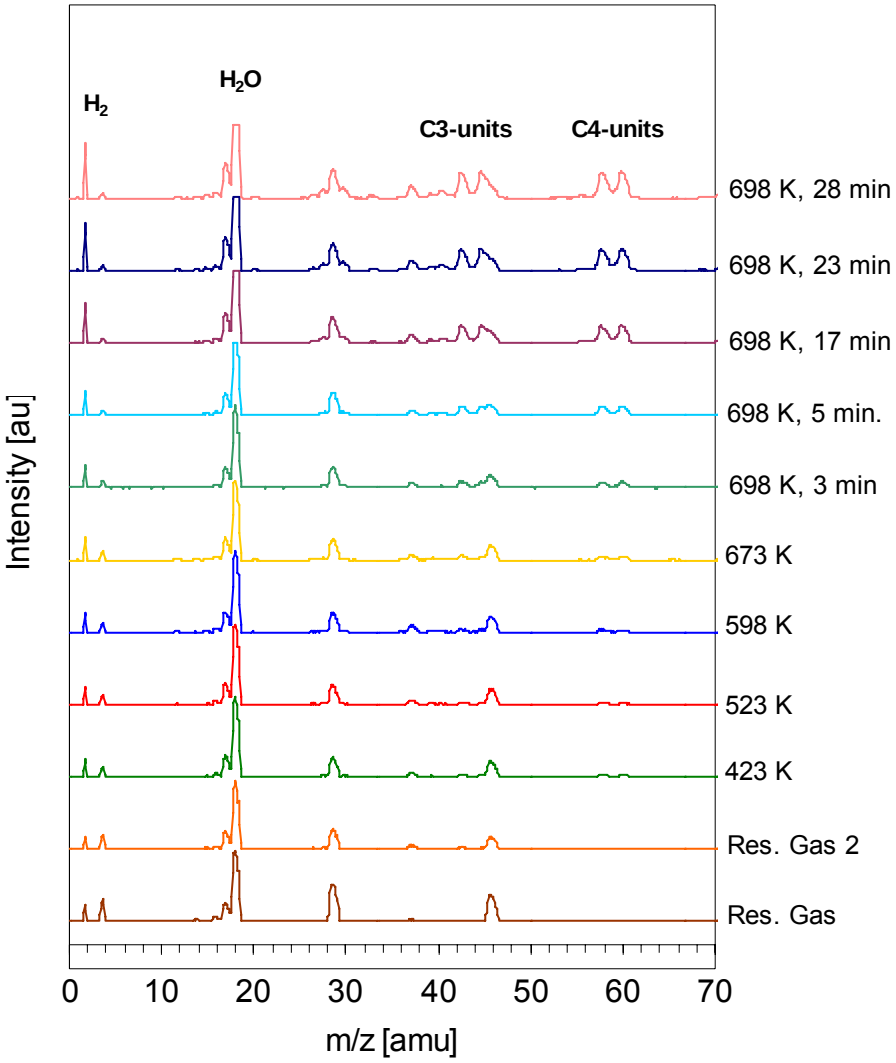

Figure 3.31: Mass spectra of fragments after dosing propene ($5 \cdot 10^{-7}$ mbar) at 300 K and annealing to higher temperatures. Residual gas is the mass spectrum of the clean vacuum, while residual gas 2 is that obtained after propene dosage.